Available online at www.sciencedirect.com
ScienceDirect
Applied Thermal Engineering 00 (2026) 1–33
Applied Thermal Engineering

An Open-Source Moving-Boundary Approach for Shell-and-Tube Heat Exchanger Sizing Optimization

Basile Chaudoir[a], Samuel Gendebien[a], Vincent Lemort[a]

[a]*Laboratory of Applied Thermodynamics, Aerospace and Mechanical Engineering Department, University of Liège, Allée de la Découverte 17, 4000 Liège, Belgium*

Abstract

Conventional single-zone heat exchanger models fail to resolve local temperature gradients, property variations, and phase transitions, while high-fidelity distributed models are often too computationally demanding to be embedded in integrated design optimization. To bridge this gap, this work presents a shell-and-tube heat exchanger sizing framework that couples a novel tube-pass-aware one-dimensional moving-boundary model with a particle swarm optimization algorithm. The modeling framework includes a user-defined discretization level, allowing a tunable balance between accuracy and computational cost. The optimization objective is the minimization of total heat exchanger mass, thereby reducing thermal inertia while lowering material use, handling requirements, and overall cost. Comparative validation against published reference cases under single-phase and two-phase operating conditions demonstrates heat exchanger mass reductions of 22 to 24%, while increasing modeling fidelity. The predictive accuracy was comparatively validated with the reference studies, with heat transfer deviations of approximately 1% and pressure-drop deviations below 10% for low discretization modeling. Achieving these improvements within a reasonable computational time, the optimization results show that the factors most strongly affecting heat exchanger mass are, in order of importance, the tube-thickness assumptions (-28 to -46%) as tubes represent 60 to 80% of the total mass, the discretization level (-10 to +56%), and the choice of objective function (-10%).

Keywords: Heat Exchangers, Particle Swarm Optimization, Shell-and-tube, Sizing, Open-source, Moving Boundary

Nomenclature

Abbreviations

ANN	Artificial Neural Network	BBO	Biogeographic-Based Opt.
FV	Finite Volumes	GA	Genetic Algorithm
HTS	Heat Transfer Search	HX	Heat Exchanger
ITHS	Intelligent Tuned Harmony Search	MB	Moving Boundary
MO	Multi Objective	NSGA-II	Non-dominated Sorting GA II
PSO	Particle Swarm Optimization	SA	Simulated Annealing
SCA	Sine-Cosine Algorithm	S&T	Shell-and-Tube

Email address: Basile.Chaudoir@uliege.be (Basile Chaudoir)

Nomenclature

Symbols			
A	Heat Exchanger Area $[m^2]$	α	Heat transfer coeff. $[W/m^2 \cdot K]$
B	Baffle Spacing $[m]$	B_o	Boiling Number $[-]$
BC	Baffle Cut $[-]$	c	Velocity constant $[m/s]$
C	Cost [$]	cp	Heat capacity $[J/kg \cdot K]$
D	Diameter $[m]$	Δ	Difference $[-]$
F	Correction factor $[-]$	f	Friction Factor $[-]$
g	Gravity constant $[m/s^2]$	G	Mass flux $[kg/m^2 \cdot s]$
h	Enthalpy $[J/kg]$	k	Conductivity $[W/m \cdot K]$
K_f	2 phase number $[-]$	L	Length $[m]$
m	Mass $[kg]$	$\dot{m}$	Mass flowrate $[kg/s]$
μ	Dynamic viscosity $[Pa \cdot s]$	n	Number of ... $[-]$
Nu	Nusselt number $[-]$	P	Pressure $[Pa]$
PEN	Penalty $[-]$	PF	Penalty factor $[-]$
Pr	Prandtl number $[-]$	q	Heat flux $[W/m^2]$
$\dot{Q}$	Heat transfer rate $[W]$	Re	Reynolds number $[-]$
ρ	Density $[kg/m^3]$	S	Surface $[m^2]$
t	Thickness $[m]$	T	Temperature $[K]$
θ	Tube layout angle [°]	U	Global heat transfer coeff. $[W/m^2 \cdot K]$
w	Cell weight coefficient $[-]$	W	Cell overlap matrix $[-]$
x	Vapor quality $[-]$	X_{tt}	Lockhart Martinelli constant $[-]$
Subscripts			
avail	Available	B	Baffle
c	Cold	cog	Cognitive
disc	Discretization	e	Equivalent
ex	Exhaust	f	Fluid / fouling
gb	Global best	h	Hot
HX	Heat exchanger	i	Inner
in	Inertial	it	Iteration
l	Liquid	mat	Material
o	Outer	p	Plate
part	Particle	pass	Tube pass per shell
pb	Personal best	s	Shell
ser	Shell in series	soc	Social
su	Supply	t	Tube
TS	Tubesheet	v	Vapor
vap	Vaporization	var	Variable
Indices			
j/k	Cell indexes	n	Iteration number
p	Particle number		

1. Introduction

1.1. Heat Exchanger Sizing Methods

Heat exchanger sizing consists of iterative steps between geometry definition phases (specifically the HX area A) and rating phases (where performance is evaluated, namely the heat rate $\dot{Q}$) [1]. The primary objective is commonly the minimization of the material and operating costs of the heat exchanger (C_{tot}), subject to the constraints of a required heat duty and on the pressure drops on both sides of the heat exchanger [2]. The complexity in heat exchanger design comes from the interdependencies among fluid conditions, heat transfer, and geometry. Classical sizing methods are widely reported in reference books [1]. However, these lack automation and focus on thermal performance, making further optimization time-consuming.

Optimizing heat exchanger sizing involves nonlinear relationships in its objective function and constraints. Consequently, nonlinear optimization methods are required to accurately capture the interactions among design variables. While these methods do not guarantee the finding of a global optimum, they can identify acceptable local optima [3]. Several numerical optimization methods have been applied to heat exchanger design, particularly for shell-and-tube heat exchangers [2]. Most rely on population-based metaheuristic algorithms. These imply the generation of a population of individuals corresponding to solution candidates. The individuals are then mutating, evolving, or moving based on the algorithm rules [4]. Although computationally intensive, their intrinsic randomness prevents the solution from being trapped in a single local optimum, while yielding several acceptable geometries. They can provide several options for adapting to the process needs. Table 1 lists several S&T HX design studies with various optimization algorithms.

Table 1: Literature review summary table on shell-and-tube heat exchanger design.

Paper	Year	HX Model	Algorithm	Objective	Main contribution
Caputo et al. [5]	2008	LMTD	GA	min(C_{tot})	Automatization of HX sizing based on total cost optimization. Result show a price reduction up to 52% compared to classical handbook approaches.
Costa et al. [6]	2008	LMTD	Oriented Search	min(A_{HX})	Introduction of discrete variable choices to provide more realistic designs.
Patel & Rao [7]	2010	LMTD	PSO	min(C_{tot})	Comparison between PSO and GA from [5]. PSO showed to yield similar results than GA with fast convergence.
Ghanei et al. [8]	2014	ε-NTU	MO-PSO	max(ε), min(C_{tot})	Multi objective optimization showing the trade-off between HX cost and effectiveness.
Turgut et al. [9]	2014	LMTD	I-ITHS	min(C_{tot})	Comparison between GA, PSO and I-ITHS. All methods yield similar results, I-ITHS showed a fast convergence even though higher number of iterations was necessary compared to PSO in [7].

Continued on next page

Paper	Year	HX Model	Algorithm	Objective	Main contribution
Caputo et al. [10]	2015	LMTD	GA	min(m_{HX})	First study focusing on mass minimization. Showing 8% to 58% mass reduction compared to commercial softwares.
Wen et al. [11]	2016	3D CFD	MO-GA	max($\dot{Q}$), min(C_{tot})	Use of CFD for the sizing optimization of S&T HX with helical baffles to find optimal helical angles.
Turgut [12]	2017	LMTD	SCA	min(m_{HX})	Sizing optimization of a S&T evaporator.
Hadidi & Nazari [13]	2019	LMTD	BBO	min(C_{tot})	Comparison of BBO with other optimization methods such as GA and PSO. All methods yield similar results and BBO showed a fast convergence time.
Nadi et al. [14]	2021	LMTD	MO-PSO	max($\dot{Q}$), min(C_{tot})	Multi-objective sizing optimization of a two-phase HX (evaporator) with a validation against experimental data.
Caputo et al. [15]	2022	LMTD	GA and MO-GA	Varied	Study aiming to compare various objective functions for shell-and-tube heat exchanger design. Using total costs or pressure drop minimization as objective provides the best design trade-off.
Xu et al. [16]	2023	ε-NTU	GA & MO-PSO	max($\dot{Q}/\Delta P$), max($\dot{Q}/m_{HX}$)	Multi-Objective optimization coupling Particle Swarm Algorithm and non-sorted Genetic Algorithm II to size small-scale S&T HX for aerospace applications.
Krishna et al. [17]	2023	2D FV	PSO	min(C_{tot})	Manufacturing cost minimization for superalloy sCO2 micro-tube S&T HX for aerospace applications. Use of a validated 2D discretized model for faster optimization compared to CFD.
Prajapati et al. [18]	2024	LMTD	MO-HTS	max(ε), min(C_{tot}), $min(\Delta Ex)$	Multi-Objective optimization study to optimize 3 objective functions (HX efficiency, total costs, exergy destruction) using a heat transfer search algorithm.
Hajabdollahi et al. [19]	2025	LMTD	Set Trimming	min(A_{HX})	Optimization of heat exchanger networks with global pressure drop constraints. Set trimming was used to find the global optimum for the sizing of each heat exchanger. The whole system was then optimized by constructing an integer linear optimization model solved with integer linear programming.

Continued on next page

Paper	Year	HX Model	Algorithm	Objective	Main contribution
Mosqueda-Huerta et al. [20]	2025	ANN (LMTD trained)	ANN (DE trained)	$\min(C_{tot})$	Training of artificial neural network for S&T HTX simulation and sizing optimization. Comparison between fully surrogate, hybrid, and rigorous sizing optimization methods. Results showed that the rigorous optimizer yielded lower total costs while using less computation time. The fully surrogate model proved to be the least efficient.

1.2. Limitations of Conventional Heat Exchanger Sizing Models

Table 1 shows that the sizing methods present in the literature predominantly rely on single-zone models such as the Log Mean Temperature Difference (LMTD) and $\varepsilon - NTU$ methods. These simplify the problem by assuming constant fluid properties along the heat exchanger. This hypothesis can lead to inaccuracies in performance prediction and sizing assessment for several flow conditions [21]. Examples are large temperature glides across the heat exchanger, multi-phase problems, and large variations of other properties with temperature (e.g., supercritical state). In contrast, most of the remaining studies use CFD (Computational Fluid Dynamics) with the aim of studying specific S&T geometries (e.g., with helical baffles) [11]. They are not always coupled with a specific optimization algorithm; sometimes, they are limited to a sensitivity analysis for computational load reduction. To the authors' best knowledge, only one study used a different heat exchanger modeling method, being 2D finite volumes (FV). The latter is coupled with PSO to provide faster than CFD, yet still detailed HX sizings [17]. Even though this method bridges between single-zone and CFD models, FV remains computationally heavy for integration into a larger optimization framework, such as a techno-economic study. A gap remains to be filled with faster yet still discretized methods, hence the choice of a moving-boundary method [22].

In addition, these modeling approaches were coupled with various optimization methods. A recent literature review fairly compared them for optimizing S&T HX [23]. It shows that the optimization algorithm chosen does not significantly impact the final value of the objective function. However, some methods have been found more computationally efficient than others using a Friedman score ranking. Differential evolution arrived first for the specific case studied, with PSO being 6th out of 20 methods. Even though the method did not reach the first place, PSO remains a well-proven, efficient, easy-to-understand, and easy-to-implement method, especially when searching over broad optimization intervals. It is also compatible with parallel processing, almost dividing the convergence speed by the number of processor cores used [24]. The current implementation of PSO also features enhancements, for example, the possibility to iterate on discrete variables as well as an enhanced space initial screening (See Section 2.2 for more details). The resulting enhanced PSO algorithm proves to be a strong choice for this study.

Finally, most previous studies minimize either the heat exchanger area or total HX cost under a specified heat duty constraint. To the best of our knowledge, few studies have focused on minimizing heat exchanger mass, which is adopted in this work as the objective function for the following reasons:

- Material mass is a key cost-driving factor in industrial design. Minimizing it can lead to favorable pricing, easier transportation and installation, and reduced material usage [10].
- The heat exchanger dynamics largely govern the dynamic behavior of thermal systems [22]; thus, reducing HX mass can enable faster transient response and improved overall system flexibility.
- The minimization of heat exchanger area or costs using area-based correlations tends to ignore important design parameters, such as tube thickness, which significantly affect HX mass and related properties.

1.3. Contributions of the proposed methodology

This paper introduces a novel, open-source shell-and-tube heat exchanger sizing framework based on a one-dimensional moving-boundary model coupled with a particle-swarm optimization algorithm and a geometry generation procedure. The proposed model adopts a one-dimensional formulation and therefore does not capture two- or three-dimensional fluid behavior; however, it still discretizes the heat exchanger and provides physically consistent sizing in any phase configuration provided case-appropriate correlations. In design contexts for which the heat exchanger must be simulated repeatedly, the moving boundary method provides significant gains in computational time compared to FV and CFD [22]. The proposed tool is well suited for integration in larger techno-economic frameworks that require discretized heat exchanger modeling.

The main contributions of this work are:

- Development of a shell-and-tube heat exchanger sizing methodology based on a flexible one-dimensional moving-boundary model with user-defined discretization, enabling a controlled trade-off between physical fidelity and computational cost.
- Generalization of the moving-boundary formulation to handle any phase configurations given an appropriate set of heat-transfer and pressure-drop correlations, enhancing adaptability to diverse process conditions.
- Enhancement of the 1D counter-flow moving boundary model to capture multi-pass geometry behavior through a geometric reconciliation algorithm.
- Introduction of a geometry generation algorithm capable of reconstructing a coherent, simulation-ready heat exchanger geometry from a reduced set of optimization variables, enabling the evaluation of thermal inertia and compatibility with dynamic simulation frameworks.
- Formulation of an enhanced particle-swarm optimization routine explicitly targeting heat exchanger mass minimization, directly linked to both capital cost and thermal inertia.
- Implementation and public release of the framework as an open-source tool within the LaboThApPy [25] environment, ensuring transparency, reproducibility, and re-usability.
- Demonstration of the proposed methodology through comparative case studies involving both sensible and latent heat transfer, illustrating its applicability and performance relative to conventional sizing approaches.
- Analysis of sizing outcomes, identifying key modeling and optimization considerations—such as tube thickness assumptions, objective function formulation, and spatial discretization level—that significantly influence heat exchanger mass.

Note that the proposed method is generic and can be applied to another type of heat exchanger. It would require identification of independent variables, geometry generation according to technology-specific standards, and heat transfer modeling of that specific geometry. In this work, only the methodology specific to shell-and-tube heat exchangers is considered.

2. Methodology

2.1. Sizing Tool

The first goal of this model is to find the appropriate heat exchanger geometry to minimize a given objective function under given constraints. The tool relies on the interactions between a PSO algorithm, a geometry generation algorithm, and a heat exchanger model. These interactions are detailed in Section 2.2. Before presenting the detailed methodology, inputs/parameters/outputs are detailed. They are represented in Figure 1.

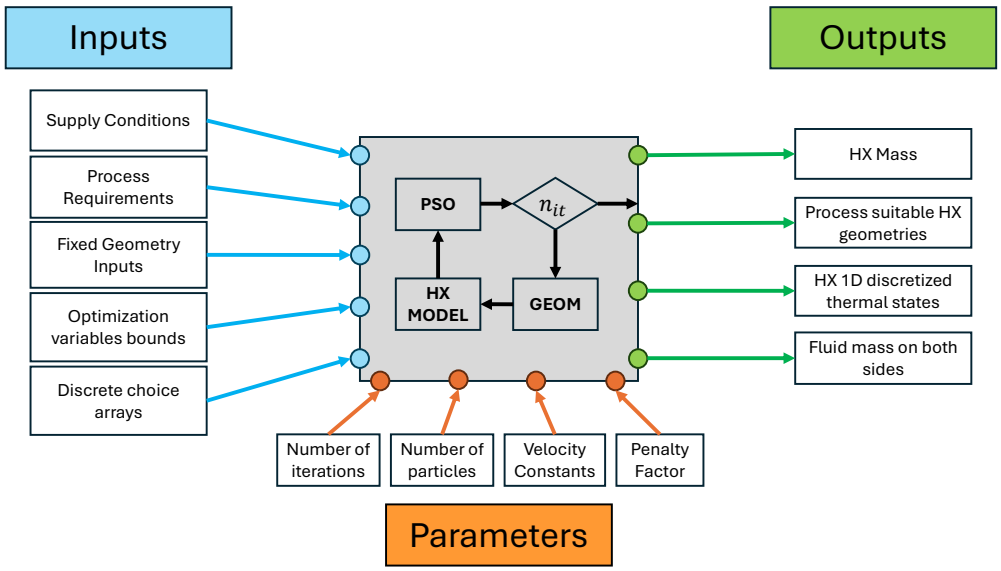

Figure 1: Schematic overview of the sizing tool with its inputs, outputs, and parameters.

Inputs:

The inputs represent the problem of the user. They consist of thermodynamic inputs linked to the process in which the heat exchanger shall be integrated, and geometrical inputs linked to the user expectations of the geometry to spatially fit the process.

Thermodynamic inputs are defined in this work for the considered study cases in Section 4. They include:

- **The supply conditions:** fluid, mass flowrates, pressures, and enthalpies. They serve as the heat exchanger model inputs.
- **Process requirements:** in terms of heat duty ($\dot{Q}_{req}$) and allowable pressure drops (ΔP_{max}). They translate into optimization constraints that shall be satisfied by the sized heat exchanger, detailed in Section 2.5.

Geometry inputs include:

- **Optimization variable limits:** either bounds for continuous optimization variables or choice arrays for discrete optimization variables, detailed in Section 2.3.
- **Fixed simulation parameters:** These are the number of shells in series and in parallel (n_{ser}, n_{para}), fouling thermal resistances (R_f), tube material conductivity (k_t) and the number of discretizations considered in the model (n_{disc}). In the present work, they are fixed for different study cases in Section 4.

Parameters:

The numerical behavior of the tool is controlled by the parameters of the PSO algorithm. They allow the tuning of the quality of solution versus computation effort trade-off. These are:

- **The number of particles (n_{part}) and the number of iterations (n_{it}):** These are directly linked to the optimization algorithm described in Section 2.2 and place the cursor on the trade-off between result accuracy and computation time.
- **The penalty factor (PF)**: It weights the penalties resulting from non-satisfaction of optimization constraints (see Section 2.5).
- **The velocity constants (c)**: These parameters weight the different velocity components to update a particle's velocity for the next iteration [26].

Outputs:

The outputs of the tool are the optimal heat exchanger parameters and the corresponding simulation results. These are:

- **The optimal heat exchanger mass (m_{HX}):** The optimization objective.
- **The fluid thermodynamic states evolution:** Along the heat exchanger depending on the discretization level.
- **Total fluid masses:** At each side of the heat exchanger (m_f), evaluated using a void fraction model.

In addition to the optimal solution, the particle swarm algorithm can provide many suitable geometries satisfying process constraints. The results associated with the suitable geometries during the optimization process can also be kept for analysis.

2.2. Algorithm Coupling

The integration of the geometry generation procedure and the heat exchanger model and the particle swarm optimization algorithm is detailed in Figure 2. The interactions with inputs, parameters, and outputs (coloured boxes representing the information detailed in Section 2.1) is also represented.

Particle swarm optimization (PSO) is a stochastic population-based approach [26]. A solution candidate corresponds to a particle position that evolves across iterations as its velocity updates. Particle velocities are updated as a sum of social, cognitive and inertial components weighted by velocity constants. Several variants of this method exist to enhance the particle search. The following modifications to the root algorithm were implemented for this work:

- **Initial Oversampling:** An oversampling factor of three was chosen from preliminary testing to balance the trade-off between initial coverage of the high-dimensional search space and computational efficiency. This means $n_{part} \times 3$ particles are first initiated and scored. The particles are then sorted such that the n_{part} best particles remain.
- **Particle re-initialization:** Particle are reinitialized to avoid stagnation in local minima. A three iteration threshold was chosen through preliminary testing to enhance exploration.
- **Discrete variable compatibility:** When a choice vector is supplied (i.e., a vector with all possible values), the algorithm can move from a discrete variable to another. This ensures realistic values of optimization variables.

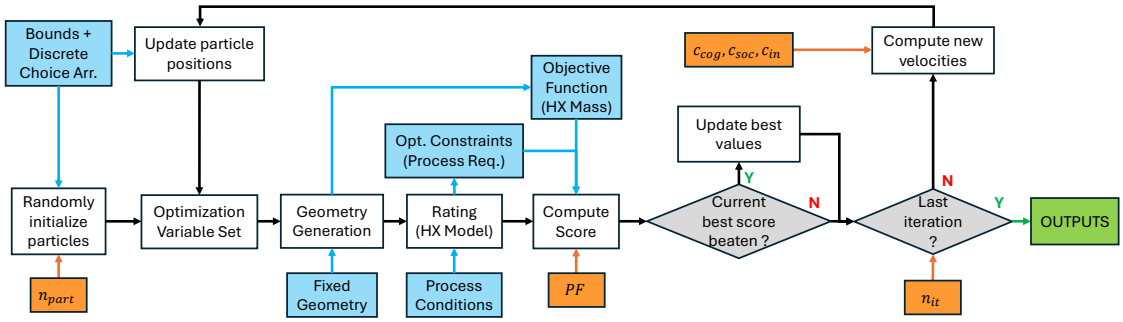

Figure 2: Flowchart of the Particle Swarm Optimization algorithm coupled with geometry generation and HX model.

2.3. Optimization Variables

Figure 3 shows a representation of the optimization, simulation and mass variables problem variables on a simplified Shell-and-Tube geometry.

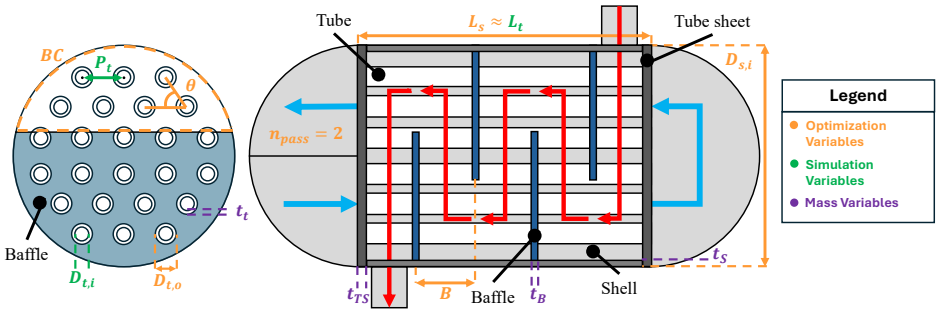

Figure 3: Optimization, simulation and mass variables represented on a simplified Shell-and-Tube geometry.

The seven optimization variables considered in this work are listed in Table 2 with their bounds. These can take either continuous or discrete values. The tube outside diameter ($D_{t,o}$) and the internal shell diameter ($D_{s,i}$) can take discrete values in inches usually found in the industry. The baffle spacing (B) is imposed to a divisor of the tube length ($L_t \approx L_s$) between given structural bounds. $n_{t,pass}$ corresponds to the number of tube passes per shell. θ is the tube layout angle that can indicate inline square (0°), staggered square (45°), and triangular (60°) configurations. Finally, the baffle cut (BC) is expressed as an area percentage.

Table 2: Optimization variables with constraints and discrete value arrays.

Variable	Unit	Type	Bounds	Constraints	Discrete value arrays
$D_{t,o}$ [1]	in.	Discrete	[0.5; 1.5]	-	[0.375, 0.5, 0.625, 0.75, 1, 1.25, 1.5]
L_s	m	Continuous	[1; 15]	$\in [3D_{s,i}; 15D_{s,i}]$, $L_t \approx L_s$	-
$D_{s,i}$ [27]	in.	Discrete	[8; 120]	-	[8, 10, 12, 13.25, 15.25, 17.25, 19.25, 21.25, 23.25, 25, 27, 29, 31, 33, 35, 37, 39, 42, 45, 48, 54, 60, 66, 72, 78, 84, 90, 96, 108, 120]
B [27]	m	Discrete	$\left[\frac{D_{s,i}}{5}; 74{D_{t,o}}^{0.75}\right]$	Divisor of L_s	-
n_{pass}	-	Discrete	[1; 10]	-	[1, 2, 4, 6, 8, 10]
θ [1]	°	Discrete	[0; 60]	-	[0, 45, 60]
BC [27]	%	Continuous	[15; 45]	-	-

2.4. Objective Function

The objective function is the heat exchanger mass, computed as in Equation 1. The variables used to compute the mass are illustrated in Figure 3.

$$m_{HX} = m_t + m_s + m_{TS} + m_B \tag{1}$$

Where the tube mass (m_t) depends on the number of tubes per shell (n_t) and the density of their material (ρ_{mat}). The material considered in this work is carbon steel (also for the other heat exchanger components), thus $\rho_{mat} = 7850\,kg/m^3$. m_t is computed as:

$$m_t = \pi \times \left(\frac{{D_{t,o}}^2 - {D_{t,i}}^2}{4} \right) \times L_t \times n_t \times n_{ser} \times n_{para} \times \rho_{mat} \tag{2}$$

The shell mass (m_s) is computed in a similar way.

$$m_s = \pi \times \left(\frac{(D_{s,i} + 2 \times t_S)^2 - {D_{s,i}}^2}{4} \right) \times L_s \times n_{ser} \times n_{para} \times \rho_{mat} \tag{3}$$

Two tube sheets per shell are considered in this work. The tube sheets mass is computed as follows:

$$m_{TS} = 2 \times \pi \times \left[\frac{{D_{s,i}}^2}{4} - n_t \times \frac{{D_{t,o}}^2}{4} \right] \times t_{TS} \times n_{ser} \times n_{para} \times \rho_{mat} \tag{4}$$

Finally, the baffle total mass (m_b) is computed as:

$$m_B = \left[\frac{{D_{s,i}}^2}{4} - n_t \times \frac{{D_{t,o}}^2}{4} \right] \times \left(1 - \frac{BC}{100} \right) \times \frac{L_t}{B} \times t_B \times n_{ser} \times n_{para} \times \rho_{mat} \tag{5}$$

The computation of the different thicknesses (the tube wall thickness (t_t), the shell thickness (t_S), the tube sheet thickness (t_{TS}), and the baffle thickness (t_B)) is detailed in the Section 2.6.

2.5. Optimization Constraints

The considered optimization constraints are listed in Table 3. If any constraints is not respected, a penalty (PEN) is computed as the difference between the required and the actual value multiplied by the penalty factor (PF). For a constrained value C with a maximum required value C_{req}, one has:

$$PEN = PF \times max((C - C_{req}), 0) \tag{6}$$

If the constraint is satisfied, $PEN = 0$. The total score of a particle is then computed as the sum of the objective function (here m_{HX}) and of all the penalties (PEN_i):

$$score = m_{HX} + \sum_i PEN_i \tag{7}$$

PF was set to a high value to eliminate geometries violating constraints (See Section 2.3). While a high penalty factor can slow convergence, the wide bounds of the optimization variables provide a sufficiently large search space to ensure finding suitable geometries for the considered study cases.

Table 3: List of design constraints used in the study with descriptions.

Design Constraint	**Constrained Value**	**Description**
Heat rate	$\dot{Q}_{HX} \geq \dot{Q}_{req}$	Required heat rate to satisfy the process requirements. Reason why the heat exchanger is used.
Pressure drops	$\Delta P_s, \Delta P_t \leq \Delta P_{max}$	Maximum allowable pressure drops limiting the mass minimization. These values can be either defined by generic guidelines [28] or through a cycle thermo-economic study.

2.6. Geometry Generation

This section aims to provide the methodology for the heat exchanger geometry generation. This part consists in finding interrelationships between variables in order to isolate independent variables (the optimization variables). Figure 4 shows the links between the geometrical variables and the path to compute a geometry allowing for mass estimation and model simulation based on a set of independent optimization variables. These variables are all represented in Figure 3 when possible; the variables in green are the ones required to simulate the heat exchanger, whereas the purple ones are directly used to compute the heat exchanger mass.

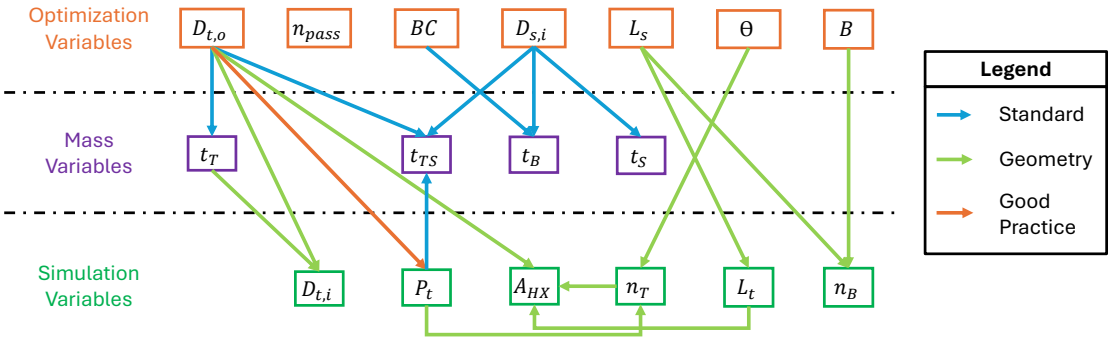

Figure 4: Arrow diagram of variable inter-dependencies for the shell-and-tube geometry generation for one shell.

Table 4 summarizes the links and computation methods of the different geometrical variables. Most of these variables depend on geometrical and mechanical constraints. The remaining variables are imposed using good practice, linking them with other variables. A corrosion allowance of 1.6 mm was added to all computed thicknesses except for tubes, as prescribed for carbon steel components by the TEMA code [29].

Table 4: Summary of geometry computations for the shell-and-tube heat exchanger.

Variable	Description	Dependency	Methodology
t_t	Tube thickness	$D_{t,o}$; $P_{su,t}$; $P_{su,S}$	Smallest thickness choice from ASME B31 [30] (based on $D_{t,o}$ for carbon steel piping) that satisfy mechanical constraints from ASME BPVC [31].
t_{TS}	Tube-sheet thickness	$D_{t,o}$; $D_{s,i}$; P_t	TEMA code expression as in [32].
t_B	Baffle thickness	$D_{s,i}$; BC; $P_{su,S}$	Method from Pressure Vessel Design Manual [33].
t_S	Shell thickness	$D_{s,i}$; $P_{su,S}$	TEMA code expression as in [32].
$D_{t,i}$	Internal tube diameter	t_t; $D_{t,o}$	$D_{t,i} = D_{t,o} - 2 \times t_t$
P_t	Tube pitch	$D_{t,o}$	Generic values from [1] which are directly linked to $D_{t,o}$.
n_t	Number of tubes	$D_{s,i}$; P_t; θ	From a in-house code filling a surface of diameter $D_{s,i}$ with tubes with a P_t spacing and arranged with an angle θ. Validated using data from [27].
n_B	Number of baffles	B; L_t	$n_B = L_t/B$
A_{HX}	Heat exchanger area	$D_{t,o}$; n_t; L_t	$A_{HX} = \frac{\pi}{4} D_{t,o}^2 \times L_t \times n_t$

3. Heat Exchanger Modeling

This section aims to present the modeling approach developed in this work. The proposed model is adapted from the plate heat exchanger formulation proposed by [34]. This LMTD-based method has proven its robustness for plate heat exchangers, and remains robust as long as the flow configurations can be assumed parallel or counter-flow. In the present study, the approach is extended to simulate discretized pressure drops and the flow configurations of shell-and-tube heat exchangers, including cases with multiple tube passes. The main novelty of this model lies in the reconciliation of the moving-boundary, counter-flow-based formulation with a multi-pass geometrical problem that is, by nature, not purely counter-flow.

3.1. Modeling Approach

The heat exchanger model employed in this work is based on a moving-boundary approach discretizing the heat exchanger into cells by enthalpy intervals [34]. Thermophysical properties are evaluated using the CoolProp library [35] at the mean inlet and outlet pressures and enthalpies of each cell. It assumes a uniform evolution of fluid properties inside the tubes and an axial evolution of properties in the shell. Based on these assumptions, the overall heat exchanger solution procedure is described below:

1. External and internal pinching are performed to find the maximum heat rate ($\dot{Q}_{max}$). At this stage, pressure drops are estimated based on supply operating conditions.

2. An iterative solving approach using the Brent's algorithm is initiated with the objective to find the root of a residual function that only depends on the total heat exchanger heat transfer rate: $r = r(\dot{Q}) = 1 - \sum_j^n w_j(\dot{Q})$. The associated w_j with cell j is defined as:

$$w_j = \frac{UA_{req,j}}{UA_{avail,j}} = \frac{A_{req,j}}{A_{HX}} \tag{8}$$

   $UA_{req,j}$ is the HX thermal conductance required to match the enthalpy difference across the j cell, while $UA_{avail,j}$ represents the thermal conductance that would be available if the cell j were to occupy the entire HX transfer area. w_j therefore corresponds to the proportion of the heat exchanger total heat transfer area (A_{HX}) required for the j cell to satisfy its heat transfer rate. Each w_j value is shared between one cell on the hot side and one cell on the cold side.

   In a counter-flow configuration, $UA_{req,j}$ and $UA_{avail,j}$ can be evaluated from the hot and cold cells facing each other. For multi-pas arrangements, the cells on both sides cannot be considered in direct geometrical opposition. In such cases, a reconciliation between the 1D discretization and the real geometry is necessary. The following presents the steps involved during each iteration.

   (a) For a given heat rate $\dot{Q}$, the heat exchanger is discretized into multiple cells based on enthalpy, while ensuring the conservation of energy between the hot and the cold sides. Figure 5 illustrates the cell division for 3 discretizations of both the hot and the cold fluids in a one-tube-pass configuration. The first division is determined by the fluid phases present under the current heat transfer rate ($\dot{Q}$). Additional divisions are then inserted based on the heat transfer rate distribution from the previous iteration until the desired number of discretizations, n_{disc}, is reached. The enthalpies on each fluid side are then sorted, yielding two enthalpy vectors ($\vec{h}_h$ and $\vec{h}_c$).

   (b) Initially, w_j values for each cell are guessed equal ($w_j = 1/n_{disc}$ for all j). In multi-pass configurations, an overlap matrix W is constructed to account for the partial geometrical alignment between tube-side and shell-side cells. Each value W_{jk} corresponds to the fraction of the total heat exchanger area associated with the overlap of a tube-side cell j and a shell-side cell k. Figure 6 represents the W_{jk} elements for a two tube pass heat exchanger with 3 discretizations. Note that for a single-pass case, W reduces to a diagonal matrix whose entries correspond to the w_j values.

(c) For each discretization, the fluid phase on both the hot and cold sides is determined based on the local pressure and enthalpy. This allows for the selection of the appropriate correlations for the heat transfer coefficient and pressure drop. Additionally, an $LMTD$ correction factor F is computed per shell using the equations from [36].

(d) Heat transfer coefficients α_c and α_h are computed based on local phase conditions in each cell. The correlations used in this work are listed in Appendix A. Once the coefficients are determined, the UA_{avail} matrix are constructed as follows:

$$UA_{avail,jk} = W_{jk} \times \left((\alpha_{c,j} \times A_c)^{-1} + (\alpha_{h,k} \times A_h)^{-1} + R_{cond} + R_{f,c}/A_c + R_{f,h}/A_h \right)^{-1} \tag{9}$$

Where the W_{jk} factor accounts for the geometrical contact between the j and the k cells. For a tube cell j, the total available conductance is obtained by summing over all shell-side cells and re-scaling to match the total heat exchanger area:

$$UA_{avail,j} = \frac{\sum_k UA_{avail,jk}}{\sum_k W_{jk}} \tag{10}$$

(e) The $LMTD$ value for each cell is then computed. For single-pass heat exchangers, it can be directly evaluated from the cell inlet and outlet temperatures, as the hot and cold side directly opposite each other. In multi-pass configurations, the j tube cell may interact with several shell cells. The $LMTD$ value for a tube cell j is then computed as a weighted sum of the $LMTD_{jk}$ values with each shell cell it faces:

$$LMTD_j = \frac{\sum_k (LMTD_{jk} \times UA_{avail,jk})}{\sum_k UA_{avail,jk}} \tag{11}$$

$LMTD_j$ thus corresponds to the equivalent value that would satisfy $\dot{Q}_j = \sum_k \dot{Q}_{jk}$. If the boundaries of overlapping j and k cells do not match geometrically, linear interpolations of the boundary temperatures are considered for the computation of $LMTD_{jk}$. Figure 7 illustrates the $LMTD$ computation for a two-tube-pass case. From the resulting $LMTD_j$, the value of $UA_{req,j}$ is calculated:

$$UA_{req,j} = \frac{\dot{m}_j (h_{j+1} - h_j)}{F \times LMTD_j} \tag{12}$$

Once all $UA_{req,j}$ and $UA_{avail,j}$ have been computed, the w_j and the residual can be evaluated.

(f) Before iterating, the pressure drops are computed per cell and the pressures are updated along the flow direction:

$$p_{h,j+1} = p_{h,j} + \Delta P_{h,j}; \;\; p_{c,j+1} = p_{c,j} - \Delta P_{c,j} \tag{13}$$

Note that the pressure drop is added for the hot side because the heat exchanger is solved in the direction of the cold-side flow, meaning that $p_{h,0} = p_{h,ex}$. The correlations for the pressure drops are listed in Appendix B.

3. The heat transfer coefficient computations may depend on the local heat flux (in W/m^2), as it is often the case for two phase heat transfer coefficient correlations [37]. In such situations, the results become sensitive on the initial guess of the w_j values. Therefore, steps (c) to (f) are then iterated using the newly computed w values until convergence is reached.

4. At each iteration, pressure drops are recomputed, which may modify the pinch conditions and invalidate the previously determined $\dot{Q}_{max}$. Once the Brent method for performance assessment has converged, a check with newly computed pressure drops ensures that the heat exchanger heat rate $\dot{Q}$ does not exceed $\dot{Q}_{max}$. If it does, a new performance assessment solving starts by bounding $\dot{Q}$ with the newly computed $\dot{Q}_{max}$.

3.2. Model Representation

Figures 5 and 6 illustrate the representation of a shell-and-tube heat exchanger with three discretizations and respectively with one and two tube pass configurations. In these figures, the shell side is the hot fluid and the tube side is the cold fluid. Shell-side properties are assumed to vary only along the axial direction.

For a single tube pass (Figure 5), the heat exchanger is treated as counterflow, and each cell on the shell side aligns directly with a corresponding tube-side cell. The model discretization ensures energy conservation cell-by-cell ($\dot{Q}_{c,j} = \dot{Q}_{h,j}$) while capturing the local variations in heat transfer.

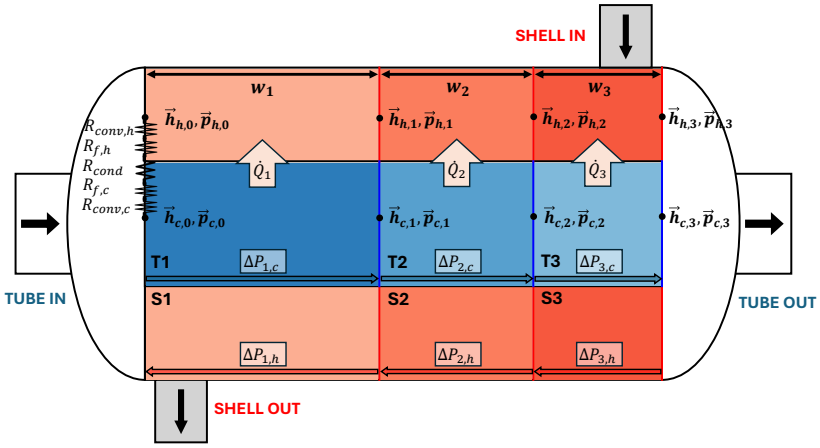

Figure 5: Schematic of a single-tube-pass heat exchanger model with three discretizations.

When multiple tube passes are considered (Figure 6), geometrical alignment between tube-side and shell-side cells is no longer ensured. Indeed, the cells on both sides still share the same heat exchanger area fraction (w) but the tube flow path is longer and folded into alternating directions. For instance, in Figure 6, $w_1 > 0.5$, meaning that the first hot and cold cells occupy more than half of the heat exchanger area. This implies that the first tube cell spans both tube passes. In this case, $\dot{Q}_{c,j} = \dot{Q}_{h,j}$ cannot be guaranteed, and the heat transfer is calculated considering the cell overlaps W_{jk}, quantifying the heat exchanger area fraction of the contact between the j tube cell and the k shell cell. Furthermore, a single shell pass is now in contact with several tube passes simultaneously.

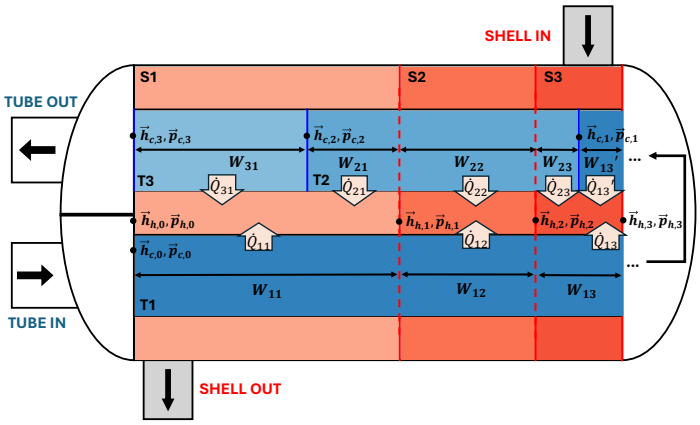

Figure 6: Schematic of a double tube pass heat exchanger model with three discretizations.

Also, the $LMTD$ computation for each cell cannot be computed when discretizations are not facing each other. Therefore, each cell is thus subdivided into subcells as illustrated in Figure 7. Using the cell bounds temperature values (in black) and linearly interpolated intra-cell temperature (in white), an $LMTD$ value is calculated for each subcell. Note that $LMTD$ values are computed considering a counter-flow arrangement for both passes, since all cells heat transfer is corrected using an F for $LMTD$ factor. It is assumed that the F factor reconciliates the assumed axial evolution of the shell flow and the real flow mixing caused by the baffles.

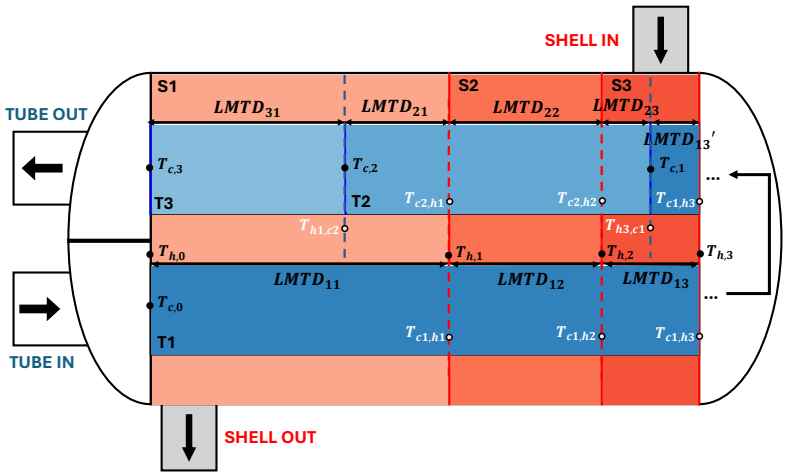

Figure 7: Representation of the LMTD computation subcells for a two-tube-pass heat exchanger with three discretizations.

4. Modeling Approach Analysis

4.1. Study Cases Presentation

This section presents the study cases used to validate the sizing tool in Section 4.2. The first case, from [5], focuses on the HX total costs optimization (directly dependent on the heat transfer area) for a sensible heat transfer from hot methanol to cold water. In the second case from [12], the HX total costs were optimized for $R134a$ at a saturated liquid state being evaporated using hotter water. These reference cases were chosen thanks to their high level of detail in intermediary computations allowing for extensive comparison and validation. More details are provided in Table 5. Since only two independent variables are required to determine the thermodynamic state in CoolProp, a pressure value was computed or selected to approach the properties from reference studies. This choice could have an impact on the results compared to those of studies [5] and [12], as discussed in Section 4.2.

Table 5: Inlet fluid conditions used for each case study.

Case Presentation	$\dot{m}$ **[kg/s]**	**Phase**$_{su}$	T_{su} **[°C]**	T_{ex} **[°C]**	p_{su} **[bar]**	R_f **[m^{2}K/W]**
Case 1						
Shell: Methanol	27.8	Liquid	95	40	10	0.00033
Tube: Water	68.9	Liquid	25	40	2	0.0002
Case 2						
Shell: Water	5.35	Liquid	26	12	2	0.000176
Tube: R134a	1.62	Liquid (x=0)	7	7	3.75 (sat)	0.000176

4.2. Modeling Approach Validation

In this section, the model is validated through comparison with reference studies through simulations using the optimal geometries reported in the original works. As the reference studies use single-zone models, an initial validation with one discretization was initially carried out. The results were compared to assess whether the models can be considered equivalent. Then, 50 discretizations were applied to evaluate their impact on the results. Consistent with the assumptions made in the reference studies, wall conductivity was neglected, and only one shell was considered. Table 6 summarizes the performance and the related heat exchanger geometries for both cases.

For the 50-discretization cases, Reynolds and Prandtl numbers, heat transfer coefficients and $LMTD$ values are reported as the weighted mean using the w values as weighting factors (see Section 3 for its definition). The relative errors ΔRef_1 and ΔRef_{50} represent the deviations of the present model from the reference results for the one- and 50-discretization models, respectively. The model enforces a minimum discretization number equal to the number of phases present. For Case 2, the case of one-discretization effectively has two discretizations. They correspond to the two-phase and the superheated single-phase region in the heat exchanger. It is thus referred as the two-discretization case.

Table 6: Model validation data compared to results of reference cases from Caputo [5] and Turgut [12].

	Case 1					**Case 2**				
	Caputo	n_{disc} = 1	ΔRef_1	n_{disc} = 50	ΔRef_{50}	Turgut	n_{disc} = 2	ΔRef_2	n_{disc} = 50	ΔRef_{50}
$D_{s,i}$ [m]	0.83					0.173				
L_t [m]	3.379					4.18				
B [m]	0.5					0.381				
$D_{t,o}$ [m]	0.016					0.01				
pitch ratio [-]	1.25					1.25				
$D_{t,i}$ [m]	0.0128					0.008				
n_t [-]	1567					230				
n_{pass} [-]	2					2				
A_{HX} [m^2]	262.8					30.2				
Re_t [-]	10936	11422	4.4 %	11778	7.7 %	N/A	-	-	-	-
Pr_t [-]	5.7	5.18	-9.1 %	5.07	-11.1 %	N/A	-	-	-	-
α_t [W/m^{2}K]	3762	3900	3.7 %	3960	5.3 %	3743	3758	0.4 %	3660	-2.2 %
Re_s [-]	11075	12193	10.1 %	13509	22 %	3018	2816	-6.7 %	2803	-7.1 %
Pr_s [-]	5.1	4.69	-8 %	4.51	-11.6 %	6.62	7.38	11.5 %	7.48	13 %
α_s [W/m^{2}K]	1740	1721	-1 %	1752	0.7 %	4719	4447	-5.8 %	4438	-6 %
$LMTD$ [K]	30.4	30.4	0 %	26.5	-12.8 %	10.5	9.9	-5.7 %	10.2	-1 %
$\dot{Q}$ [kW]	4340	4380	0.9 %	4137	-4.7 %	313	313	0 %	315	0.6 %
ΔP_t [Pa]	4298	4253	-1%	4124	-4 %	21755	19778	-9.1%	28730	32.1 %
ΔP_s [Pa]	13267	13526	2 %	13443	1.3 %	8235	8704	5.7 %	8597	4.4 %

For Case 1, the 1-discretization exhibits behavior similar to that of the reference model. The values of ΔRef_1 indicate that non-negligible differences may arise in property evaluation, even though identical thermo-hydraulic correlations are employed. While the reference case assumes fixed fluid property values, the present model computes these values using the CoolProp library [35]. This difference, however, does not significantly affect the predictions. On the other hand, the values of ΔRef_{50} show the effect of the non-constant properties along the heat exchanger. Notably, the $LMTD$ (corresponding to an equivalent perceived value for the 50 discretization case) differs by more than 10%. This directly impacts heat transfer rate and the local fluid properties. A more detailed discussion of this behavior is provided in Section 4.3. Despite

this, pressure drops remain in agreement with the reference values.

For the two-phase case (Case 2), different correlations were employed to ensure numerical stability. The Gungor-Winterton correlation used by the reference study showed unstable behavior when applied in a discretized model, especially when close to saturated vapor state, with heat transfer coefficients diverging to very large values. The Borishanskii correlation from [37] was adopted instead and improved convergence. The Kern method referenced in Case 2 contained differences in intermediate calculations compared to Case 1. The empirical correlations from Case 1 were retained to maintain methodological consistency (See Appendix A for the formulation). Finally, the R134a flow was divided into two zones due to the presence of superheated vapor in the heat exchanger.

The model predicted a similar heat transfer and pressure drops, with the main deviation being the evaporation pressure drops, underestimated by about 9 %. This deviation is still assumed reasonable for heat exchanger sizing. The LMTD value of the two-discretization model showed a divergence of about 6%. Also, the value of the LMTD correction factor F was computed at a higher value by the model than for the reference case. This is why the heat rate remains similar while the mean heat transfer coefficients and the mean $LMTD$ are lower. When the model is discretized, the mean $LMTD$ rises of about 5% (see Section 4.3 for a detailed discussion). The heat rate and the shell-side pressure drops remain in good accordance with the reference. However, the evaporation pressure drops increase by more than 40% compared to the two-discretization case. This is attributed to the variation of fluid properties across discretizations coupled to the high sensitivity of the correlation employed. Note that tube Reynolds and Prandtl numbers have not been computed for this case, as the two-phase correlation used does not rely directly on these values. Furthermore, indicative values of Reynolds and Prandtl numbers could not be obtained from the reference study [12], limiting the possibility of comparative validation using these variables.

Overall, the validation results confirm that the model presented in Section 3 can accurately reproduce both single-phase and two-phase flow conditions compared with the reference studies. In the low discretization cases, relative errors remain below 1% for heat transfer rates and below 10% for pressure drops. These discrepancies can be attributed to the use of a different property database and, in Case 2, to the use of different correlations to maintain model robustness and consistency. Dividing the model into 50 cells highlights the impacts of discretizations:

- **Impact of geometry on heat transfer:** Both cases have a two-tube pass configuration. Discretization reveals the actual contact regions of the evolving fluids, which had a significant effect for Case 1. The perceived $LMTD$ varied of more than 10% from the one-discretization case compared to the 50-discretizations one.
- **Impact of evolving fluid properties:** Variations in fluid properties can explain the deviation of evaporation pressure drops in Case 2, which may have consequent sizing implications if these pressure drops become a limiting constraint.

More application cases of this model can be found on the LaboThApPy GitHub Repository.

4.3. Discretized Model Behavior

Figure 8 shows the heat transfer rate and pressure drops on both sides of the simulated heat exchangers for both cases, with 1 to 50 discretizations. For Case 1, the first 10 discretizations significantly affect the heat transfer, whereas pressure drops remain almost constant. This trend arises because the HX discretized model captures the geometry of the heat exchanger better, which impacts the perceived $LMTD$. For Case 2, convergence evaporation pressure drops is observed after 30 discretizations. This is due to variation of properties in the heat exchanger being captured. Also, the heat transfer rises slightly above the reference value when the heat exchanger has more than 30 discretizations. This number of discretizations seems to be the threshold for which the model attributes a small but non-negligible part of its heat exchanger area to the superheated region.

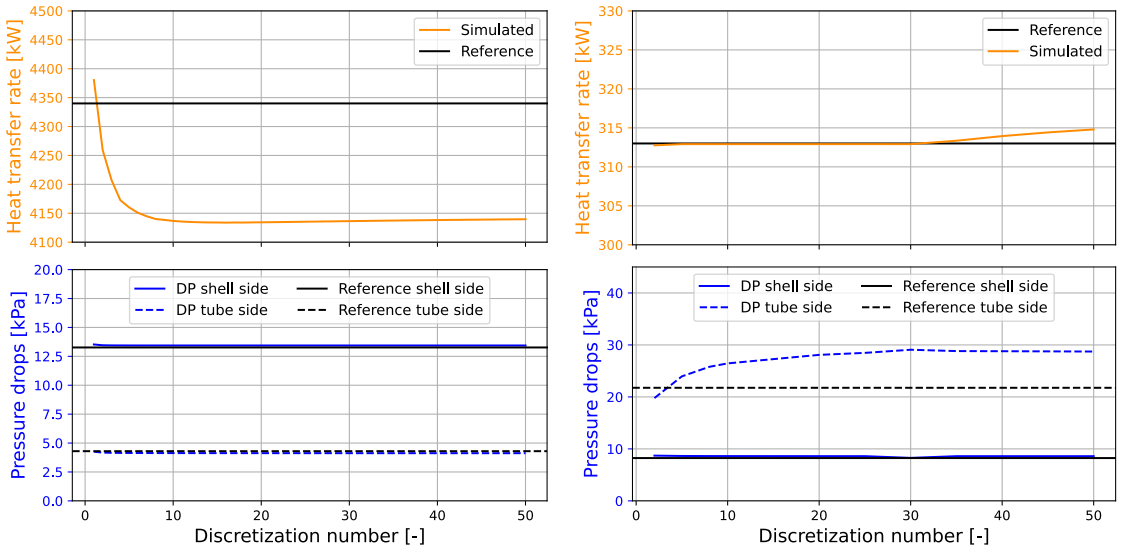

Figure 8: Heat exchanger model integral results versus discretization number for Case 1 (left) and Case 2 (right).

To illustrate the impact of the geometry on the perceived $LMTD$, Figure 9 shows the $LMTD$ value for each cell at several discretization levels, revealing the two-tube pass configurations for both cases. The more the heat exchanger is discretized, the more the profile converges towards a stable pattern. Indeed, the 30- and 50-discretization models show small differences, indicating convergence. The profiles of Case 1 show that the $LMTD$ of the last subcell (at the tube-side outlet) decreases with the number of discretizations, highlighting the pinch point location and the better capture of its temperature difference value with increasing discretization number. The position of the maximum cell $LMTD$ depends on the thermal capacity rates ($= \dot{m} \times cp$) of both fluids. The average values of these curves provide an estimate on the perceived heat exchanger $LMTD$, demonstrating its dependence on the discretization level.

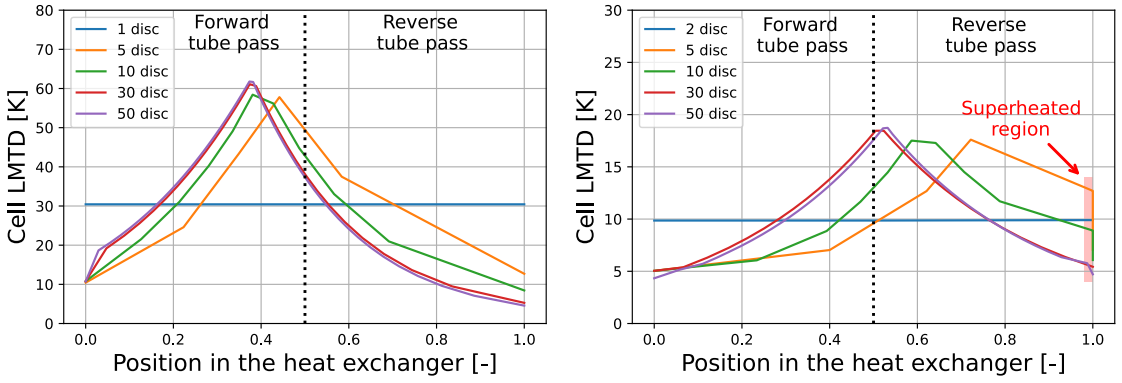

Figure 9: LMTD values over cells versus discretization number for Case 1 (left) and Case 2 (right).

Finally, Figure 10 shows the evolution of heat transfer coefficients along a 50-discretizations heat exchanger for both cases. The effect of discretizations is limited for Case 1. Indeed, the shell-side heat transfer coefficient varies from 1600 to 1800 $W/(m^2K)$, while the tube-side varies from 3500 to 4250 $W/(m^2K)$. Although these variations are not negligible, they are still nearly equivalent in average to values of the 1-discretization case, and they do not introduce a significant difference in overall heat transfer resistance.

For Case 2, Figure 10 shows that the effect of discretizations on the tube side is non-negligible. The heat transfer coefficients values vary between 3300 and 4400 $W/(m^2K)$ in the two-phase region and lie around 500 $W/(m^2K)$ in the superheated region. On the shell side, the heat transfer coefficient stays stable between 4250 and 4600 $W/(m^2K)$.

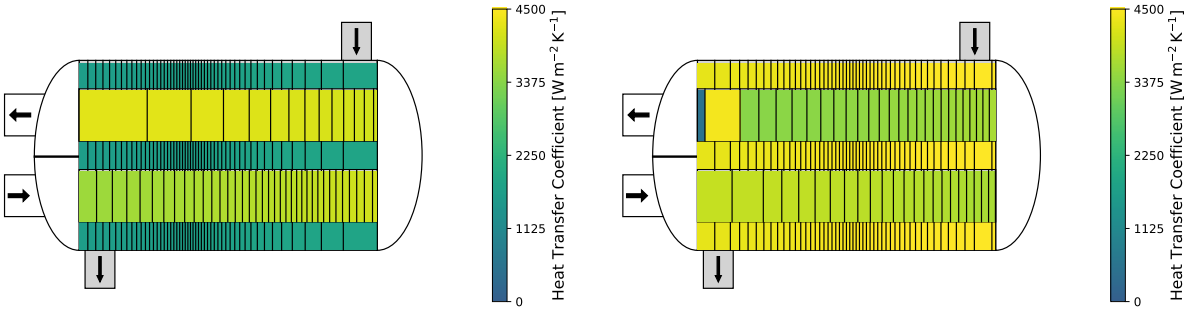

Figure 10: Heat transfer coefficient evolution for Case 1 (left) and Case 2 (right) for a 50-discretization model.

Overall, the results show that increasing the number of discretizations introduces variations in local heat transfer predictions. For Case 1, these variations remain limited and shall have negligible influence on global performance. For Case 2, however, the heat transfer coefficient varies significantly from the beginning to the end of the evaporation region, and the superheated vapor region exhibits substantially lower coefficients. This behavior reflects a stronger dependence of heat transfer on thermophysical property changes during phase transition.

For a hypothetical design case involving large superheating and/or subcooling regions (which have not been reported in the literature to our best knowledge), the single-phase portions could significantly affect the overall performance. Under such conditions, the modeling approach described in [12] (Case 2 reference) may become inaccurate, potentially leading to noticeable errors in sizing results. These findings highlight the importance of spatial resolution when modeling systems with strong temperature gradients or phase changes, as adequate discretization ensures more accurate and physically consistent predictions.

5. Optimization

The optimization of the two test cases first requires defining constraint values for the heat exchanger performance indicators listed in Table 3. For both cases, the same required heat transfer rate was imposed, while the allowable pressure drops on the tube and shell sides were fixed to the values obtained from the corresponding reference studies. The resulting optimization constraints are summarized in Table 7.

Table 7: Optimization constraints for each test case.

Case	$\dot{Q}_{req}$ [kW]	$\Delta P_{t,max}$ [Pa]	$\Delta P_{s,max}$ [Pa]
1	4340	4298	13267
2	313	21755	8235

To perform the sizing optimization, optimization parameters must be set. In the present study, baseline values were deliberately used, as the primary objective is to isolate and highlight the impact of several heat exchanger sizing considerations on the optimization results. Since the PSO algorithm is not deterministic, introducing more degrees of freedom could further amplify variability between runs and prevent meaningful

comparisons with reference studies. The optimization parameters used in all simulations are reported in Table 8.

Table 8: Optimization parameters summary for both cases.

$\mathbf{n_{it}}$	$\mathbf{n_{part}}$	$\mathbf{c_{cog}}$	$\mathbf{c_{soc}}$	$\mathbf{c_{in}}$	**PF**
50	50	0.5	0.5	0.5	10

During the simulation campaign, several heat exchanger sizing considerations were investigated:

- **The heat exchanger discretization:** The heat exchanger was optimized considering either a low discretization number (1 or 2, depending on the case), or a refined discretization with 30 cells.
- **Tube thickness computation:** The tube thickness was either assumed equal to $0.1 \times D_{t,o}$ as in the reference studies (`REF`), or computed from the standard mentioned in Section 2.6 (`STD`).
- **Tube pass number:** The tube pass number was either forced to two (`=2`), as in the reference studies, or treated as an optimization variable (`OPT`).

For each combination of these assumptions, 30 optimizations were run, and the best solution was retained. Detailed results are available in Appendix B, while the following sections present the main findings and discuss their implication.

5.1. Case 1 Discussion

Table 9 summarizes the optimization results for Case 1. Heat exchanger mass relative deviations are computed with respect to the OPT1 scenario ($\Delta m_{HX,OPT1}$). The REF and OPT1 cases differ only in the heat exchanger modeling approach (single-zone vs. single-discretization moving-boundary) and in the objective function (total cost vs. heat exchanger mass).

Table 9: Summarized optimization results compared with reference case 1 [5].

	Caputo	OPT1	OPT2	OPT3	OPT4	OPT5	OPT6	OPT7	OPT8
n_{disc}	1	1	1	1	1	30	30	30	30
t_t Comp.	REF	REF	REF	STD	STD	REF	REF	STD	STD
$n_{t,pass}$ choice	=2	=2	OPT	=2	OPT	=2	OPT	=2	OPT
n_{pass} [-]	2	2	1	2	1	2	2	2	2
A_{HX} [m^2]	262.8	292.1	208.6	239.5	217	462.7	471.8	453.7	458.8
$LMTD$ [K]	30.4	30.8	30.6	31.0	30.4	19.1	18.9	19.2	19.2
m_{HX} [kg]	3782	3355	1839	1861	1411	5234	5331	2830	2859
$\Delta m_{HX,OPT1}$ [%]	11.3	0	-45.2	-44.5	-57.9	56	58.9	-15.6	-14.8
$\frac{A_{HX}}{m_{HX}}$ [m^2/kg]	0.069	0.087	0.113	0.129	0.154	0.089	0.117	0.161	0.16

The results show that replacing a cost-based (area-based) objective function with direct mass minimization, combined with a change in heat exchanger modeling, leads to an 11.3% reduction in heat exchanger mass. This demonstrates that minimizing heat exchanger area does not necessarily lead to minimum heat exchanger mass. Different combinations of optimization variables can therefore yield substantially different masses, even when the resulting heat transfer areas remain comparable. This behavior is further illustrated

by the specific area $\left(\frac{A_{HX}}{m_{HX}}\right)$ which serves as an indicator of both cost efficiency and thermal reactivity. Since heat exchanger mass is directly related to cost, and the wall thermal time constant s inversely proportional to the specific area as defined in [38] $\left(\tau = \frac{m_{HX} \times cp_{HX}}{\alpha \times A_{HX}}\right)$. A larger specific area corresponds to more cost-efficient and more thermally reactive heat exchangers. More generally, the observed variability of the specific area confirms that heat exchanger area and mass are not proportional quantities, highlighting that mass-based optimization can be more restrictive than area-based optimization.

In the following discussion, the OPT1 configuration serves as a new reference, as it enables a clearer isolation of additional considerations. For Case 1, the three considerations introduced at the end of Section 5 have a significant impact on optimal heat exchanger mass.

- **The heat exchanger discretization** alone increases the heat exchanger optimal mass by 56%. This increase is attributed to the reduction in perceived $LMTD$ discussed in Section 4.3, where increasing segmentation to 30 elements reduced heat transfer rate from 4380 kW to about 4140 kW. Since the required heat transfer rate is fixed, the optimizer compensates by increasing the heat transfer area by 58.4%. This substantial increase in area suggests the presence of a small temperature pinch in the discretized two-pass configuration, as indicated by the significantly lower perceived $LMTD$.
- **The tube pass number variation** shows different behaviors whether the heat exchanger is discretized.
  - When one discretization is considered, the problem is bound by the tube-side pressure drops. In this case, reducing the tube pass number improves heat transfer by changing the flow configuration closer to counter-flow without changing the heat transfer coefficients significantly. As a result, the $LMTD$ correction factor F approaches unity, reducing the required conductance and the required heat transfer area. In addition, the tube-side pressure drops decrease for a given tube length. These combined effects decrease the heat exchanger area of 28.6% and the heat exchanger mass of 45.2% when comparing OPT1 and OPT2.
  - When the heat exchanger is discretized, the optimization becomes heat transfer bound for the same reasons discussed in the discretization analysis. In this situation, a two-tube pass geometry can optimize heat transfer while remaining under the pressure drop constraints. Consequently, allowing the tube pass number to vary has a negligible effect, as evidenced by the minimal differences between OPT5 and OPT6, as well as between OPT7 and OPT8.
- **The tube thickness computation rule** has a straightforward effect on heat exchanger mass. Since the assumption from the reference studies overestimates the required tube thickness, the heat exchanger mass drops significantly when the tube thickness is computed using standards from Section 2.6. Thermo-hydraulic performances were not affected significantly. The resulting mass reductions are 44.5% and 45.9% for one (OPT3) and 30 discretizations (OPT7), respectively.

When cumulating all these considerations, the optimized heat exchanger mass reaches about 2830 kg (since OPT7 and OPT8 can be considered equivalent). This corresponds to mass reductions of 14.8% and 25.2% relative to OPT1 and REF, respectively. These results demonstrate that even for a sensible heat exchanger configuration, incorporating discretization into the sizing process has a substantial impact on optimal design outcomes.

5.2. Case 2 Discussion

Table 10 summarizes the optimization results for Case 2, using the same metrics as in Table 9. A comparison between the reference case and OPT1 indicates that the present modeling approach predicts a lower $LMTD$ than the single-zone model. This difference arises from the two-zone discretization of the heat exchanger, which reduces the locally perceived temperature driving forces. The resulting 9.2% decrease in $LMTD$ requires a 17.6% increase in HX area in OPT1 to meet heat transfer requirements. As a result, the

heat exchanger mass increases by 21.5%, despite a higher specific area $\left(\frac{A_{HX}}{m_{HX}}\right)$. This behavior isolates the modeling approach—rather than the optimization objective—as the primary cause of the observed mass increase.

Moreover, some inconsistencies were noted in the reference case geometry. Specifically, the heat exchanger area reported in the reference study is approximately twice the value that can be inferred from the published geometric parameters. This discrepancy was interpreted as a likely typographical error in the reported number of tube passes, which was assumed to be two to reconcile the reported heat transfer performance and pressure drop levels. Under this interpretation, certain geometric constraints, such as the shell diameter, appear to become limiting. Accordingly, the optimization studies presented here were conducted using the interpreted reference geometry, which was assumed to be internally consistent.

Table 10: Summarized optimization results compared with reference case 2 [12].

	Turgut	OPT1	OPT2	OPT3	OPT4	OPT5	OPT6	OPT7	OPT8
n_{disc}	1	1	1	1	1	30	30	30	30
t_t Comp.	REF	REF	REF	STD	STD	REF	REF	STD	STD
$n_{t,pass}$ choice	=2	=2	OPT	=2	OPT	=2	OPT	=2	OPT
n_{pass} [-]	2	2	1	2	1	2	2	2	2
A_{HX} [m^2]	30.2	35.5	33.3	34.5	32.1	31.8	31.8	32.2	31.8
$LMTD$ [K]	10.9	9.9	10.2	9.8	10.3	10.4	10.2	10.2	10.4
m_{HX} [kg]	270	328	307	229	212	294	294	214	211
$\Delta m_{HX,OPT1}$ [%]	-21.5	0	-6.4	-30.2	-35.4	-10.4	-10.4	-34.8	-35.7
$\frac{A_{HX}}{m_{HX}}$ [m^2/kg]	0.072	0.108	0.108	0.15	0.151	0.108	0.108	0.151	0.15

For Case 2, the three considerations enumerated at the end of Section 5 also have a significant impact on optimal heat exchanger mass:

- **The heat exchanger discretization** tends to reduce heat exchanger mass, in this case. This is consistent with the results from Section 4.3, where the perceived $LMTD$ increased with the discretization number. Considering discretization alone leads to a 10.4% reduction in mass.
- **The tube pass number variation** again depends on whether the heat exchanger is discretized.
  - When two discretizations are considered, the optimization is constrained by tube-side pressure drops. Considering one tube pass enables a smaller area to satisfy both heat transfer rate and pressure drop constraints, similarly to Case 1. The OPT2 optimization shows a 6.4% mass reduction compared to OPT1.
  - When the heat exchanger is discretized, having two tube passes increases the perceived $LMTD$ while keeping pressure drops within an acceptable limit. This allows the heat exchanger to be sized with a lower heat exchange area, reducing mass. As a result, OPT5 and OPT6 results are very close. The same conclusion can be drawn for OPT7 and OPT8.
- **The tube thickness computation rule** has a similar effect as for Case 1. Using the pressure-based standard reduces heat exchanger mass by 35.4% and 28.2% for two (OPT3) and 30 discretizations (OPT7), respectively.

5.3. Heat Exchanger Mass Impacting Considerations

In previous sections, the main factors affecting heat exchanger mass have been identified and quantified for both test cases. The most influential factor is the assumption on the tube thickness computation, which had substantial effect on both cases. To illustrate its importance, Figure 11 presents the heat exchanger mass fractions by component for the results of REF, OPT1, and OPT3 listed in Tables 9 and 10. Tube mass is by far the largest contributor to the total mass, accounting for 62% to 80%. This explains the strong sensitivity of HX mass on the tube thickness. The second most important component is the shell (16% to 34 %), followed by the tube-sheets (1% to 6%) and then the baffles (≈ 1%).

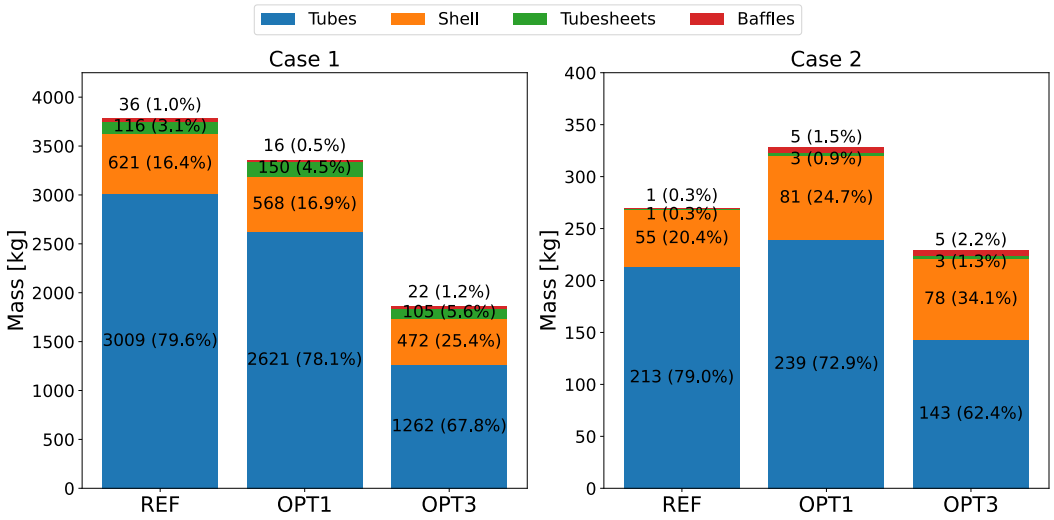

Figure 11: Mass breakdown for reference and optimized sizings (OPT1 and OPT3) of Case 1 (left) and Case 2 (right).

The second most important consideration is the discretization level, which also has the greatest impact on optimization computing time. Figure 12 presents the optimal mass and computation time evolution for both cases with the number of model discretizations. To isolate the effect of discretization, the tube pass number was fixed to two. The minimum optimized mass was chosen based on 10 runs to try to minimize the variability introduced by the stochastic optimization method.

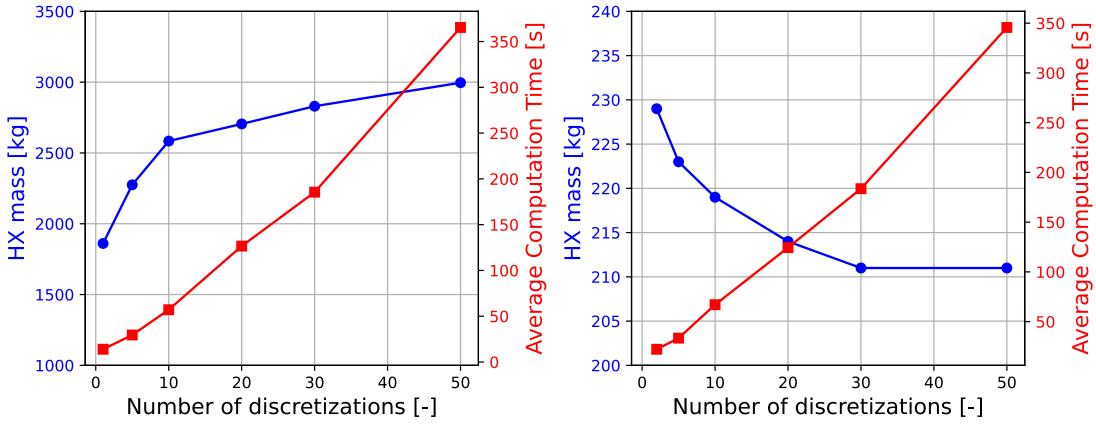

Figure 12: Optimal mass and average optimization times for Case 1 (left) and Case 2 (right).

Considering Case 1, the optimal heat exchanger mass converges at a high discretization number. This behavior can be attributed to the problem statement: when two tube passes are considered, a very tight pinch establishes at the tube side exit (around 0.5 K). In this situation, the optimizer attempts to size a highly efficient heat exchanger, and the optimal mass becomes highly sensitive to the discretization level. Increasing the number of discretizations allows the model to better resolve this temperature pinch, resulting in an increase in the predicted optimal mass. This finding aligns with the conclusions of [39] and confirms the necessity to employ a discretized model when several tube passes are considered for sizing highly efficient heat exchangers.

For Case 2, the optimal mass decreases smoothly between 2 and 20 discretizations as the perceived $LMTD$ rises. The sizing results converge at around 30 discretizations, in accordance with $LMTD$ convergence observed in Figure 9. It can be concluded that the appropriate discretization number when using this tool is case dependent.

Computation times were measured with the Python *time* library. All optimizations were executed on a laptop equipped with an Intel Core i5-11300H processor (4 cores and 8 threads at 3.1 GHz), and with 32 GB of DDR4 RAM at 3.2 GHz. Linear regression of computation time versus discretization level yielded R^2 values of 0.99 for both cases, confirming a strong linear relationship.

To conclude the discussion, Table 11 summarizes the main considerations highlighted in this study and their impact on HX mass. Other factors, such as the choice of property database or different correlations, also impact sizing results but are considered predictable and are therefore not included.

Table 11: Summary of heat exchanger sizing consideration and their impact on the resulting m_{HX}.

Consideration	**Impact**	**Occurrence**	**Explanation**
Tube thickness assumption	High (-46% to -28%)	Consistently	Tubes account for 60-80% of the total HX mass. Using pressure-based standards significantly reduces tube thickness compared to reference assumptions.
Discretization	Medium-High (-10% to +56%)	Case Dependent	Reveals internal pinch points not captured by single-zone models ($LMTD$, $\varepsilon - NTU$ [39]), especially for multi-pass HX. Captures fluid property variations affecting thermo-hydraulic performance.
Objective Function	Medium (-11%)	Consistent	Optimizing heat exchange area does not necessarily minimize HX mass. When pressure drops are fixed, mass-based optimization is more restrictive.
Tube pass count	Low-High (-45% to +0%)	Case dependent	Effect depends on discretization and constraints. Should be considered with discretized models for efficient HX sizing.

5.4. Discussion on Tool Scalability

The present method demonstrates the ability to provide shell-and-tube heat exchanger sizings with a tunable balance between computational cost and result precision. The number of function calls per model evaluation is relatively small compared to other discretized modeling approaches [22]. However, when integrating this model into larger optimization frameworks, the total number of evaluations may still pose computational challenges. To enhance efficiency and scalability, several modifications can be considered:

- **Discretization number adjustment:** A preliminary sensitivity study can help identify an appropriate discretization level that balances accuracy and computation time
- **Patience term implementation:** In Particle Swarm Optimization, the final solution may be reached well before the maximum iteration limit [7]. Implementing a stopping criterion based on lack of improvement in the objective function can significantly reduce computation time.
- **Parallel processing implementation:** Each particle in the PSO algorithm is independent and can be evaluated on a separate processor core or thread, potentially reducing computation time proportionally to the number of available cores or threads [24].

With these modifications, the tool becomes computationally efficient enough for integration into larger optimization frameworks. Additionally, the LaboThApPy environment [25] provides a thermodynamic cycle solving and optimization framework, facilitating seamless integration of the present tool into heat exchanger network and techno-economic optimization studies.

6. Conclusion

This work proposed a novel heat exchanger sizing methodology based on a tube-pass-aware, one-dimensional moving boundary model aimed at minimizing heat exchanger mass. In contrast to conventional single-zone approaches, the method captures axial variations of temperature and fluid properties while remaining computationally efficient and suitable for integration into large-scale optimization frameworks. The use of standardized geometrical correlations ensures the practical relevance of the resulting designs

The model was validated against two previously published optimization case studies involving both sensible and latent heat transfer. For low discretization levels, deviations remained below 1% for heat transfer rates and 10% for pressure drops, confirming the validity of the modeling approach. Sensitivity analyses further demonstrated that discretization strongly affects predicted local temperature differences, phase distributions, and fluid properties, with direct implications for performance and pressure-drop prediction, particularly under two-phase flow conditions.

Optimization results quantified the impact of key modeling choices on the optimal heat exchanger mass. Variations in modeling assumptions led to mass changes ranging from -11% to +22%, while discretization level and tube-pass configuration induced variations of -10% to +56% and 0% to +45%, respectively. Notably, tube thickness assumptions alone were found to consistently induce mass variations between -28% and -46%, highlighting that structural modeling choices can dominate the overall heat exchanger mass. These findings also indicate that mass minimization is inherently more restrictive than area minimization for given pressure-drop constraints and should therefore be preferred when thermal inertia or structural limitations are critical design drivers. Moreover, the results demonstrate that using a discretized model is crucial when designing highly efficient heat exchangers. This is particularly important for multiple tube-pass configurations, as internal local pinch points can appear and remain undetected by single-zone models.

Overall, the proposed methodology enables accurate and computationally efficient heat exchanger sizing and optimization, particularly for applications involving strong property variations or phase change. The current model assumes an axial evolution of shell-side properties; incorporating shell-side flow non-uniformity and baffle effects, supported by experimental validation, constitutes an important direction for future work. Extending the approach to other heat exchanger types and operating regimes, such as finned-tube or supercritical systems, would further enhance its applicability.

Model Availability

The full implementation of the present sizing model is available as an open source tool, which is part of the LaboThApPy library [25]. It can be found in the sizing section in the following repository (under

Apache 2.0 license): LaboThApPy GitHub Repository - `https://github.com/LaboThapPythonLibrary/LaboThapLibrary`.

Appendix A: Heat Transfer Modeling

The model described in Section 3.1 can simulate any phase configuration. A heat transfer correlation for any possible phase condition is thus listed in Table A1. For the shell-side, Kern was considered instead of Bell-Delaware as the latter's correction factors depend on too many variables [1]. This could lead to an optimization with too many independent variables that could drastically increase computation time and optimization complexity.

Table A1: List of the different Nusselt number and heat transfer coefficient correlations.

Side	Phase	Name	Correlation
Tube	1-Phase ($Re < 2300$)	Stephan-Preußer [5]	$Nu = 3.657 + \frac{0.0677\left(RePr\frac{D_{t,i}}{L_{t,tot}}\right)^{4/3}}{1+0.1Pr\left(Re\frac{D_{t,i}}{L_{t,tot}}\right)^{0.3}}$
	1-Phase ($2300 \leq Re \leq 10000$)	Gnielinski [40]	$Nu = \frac{(f/8)(Re-1000)Pr}{1+12.7(f/8)^{0.5}(Pr^{2/3}-1)}\left(1+\frac{D_{t,i}}{L_{t,tot}}^{2/3}\right)\left(\frac{Pr}{Pr_w}\right)^{0.11}$ $f = (1.82 \times log_{10}(Re) - 1.64)^{-2}$
	1-Phase ($Re > 10000$)	Sieder-Tate [5]	$Nu = 0.027Re^{0.8}Pr^{1/3}\left(\frac{\mu}{\mu_w}\right)^{0.14}$ $Re = \frac{n_{t,pass}}{n_{ser}}\frac{\dot{m}}{n_t\pi(D_i/2)^2}\frac{D_{t,i}}{\mu}$ $L_{t,tot} = L_{tube}\, n_{t,pass}\, n_{ser}$
	Boiling	Borishanskii et. al. [37]	$h = h_0 C_F \left(\frac{q}{q_0}\right)^n F_p F_d F_W F_{mx}$
	Condensing ($Re_v = \frac{\rho_v u_v D_{t,i}}{\mu_v} < 35000$)	Dobson-Chato [41]	$Nu = 0.555\frac{\rho_l g(\rho_l-\rho_v)h'_{vap}D_{t,i}^3}{\mu_l k_l (T_{sat}-T_w)}$ $h'_{vap} = h_{vap} + 0.375cp_l(T_{sat}-T_w)$
	Condensing ($Re_v \geq 35000$)	Dobson-Chato [41]	$Nu = 0.023Re_{D,l}^{0.8}Pr_l^{0.4}\left(1+\frac{2.22}{X_{tt}^{0.89}}\right)$ $Re_{D,l} = \frac{4\dot{m}(1-x)}{\pi D_{t,i}\mu_l}$
Shell	1 or 2 Phases ($Re < 2000$)	Kern [42]	$Nu = 0.472Re^{0.528}Pr^{1/3}$
	1 or 2 Phases ($Re \geq 2000$)	McAdams [5]	$Nu = 0.36Pr^{1/3}Re^{0.55}\left(\frac{\mu}{\mu_w}\right)^{0.14}$

The Borishanskii correlation's heat transfer coefficient is computed using many coefficients. These are calculated to express the deviations from standard conditions for a studied fluid. These standard conditions correspond to a given heat transfer coefficient (h_0) and heat flux (q_0). The heat transfer coefficient is then directly computed. All the other correlations compute a Nusselt number (Nu) used to calculate the heat transfer coefficient in tubes as follows:

$$h_t = Nu_t \frac{k}{D_{t,i}} \tag{14}$$

For the shell side, more details are required concerning the computation of the Reynolds number (Re). First, the flow velocity is computed using the equivalent flow surface (S_{flow}), where P_t is the tube pitch [43].

$$S_{flow} = \frac{D_{s,i} \times B \times (P_t - D_{t,o})}{P_t} \tag{15}$$

$$v_s = \frac{\dot{m}_s}{S_{flow} \times \rho_s} \tag{16}$$

The Reynolds number is computed by considering an equivalent shell diameter ($D_{s,e}$) also depending on the tube pitch (P_t) and the tube layout angle (θ) [43].

$$D_{s,e}(\theta) = \begin{cases} 4\dfrac{P_t^2 - \dfrac{\pi}{4}D_{t,o}^2}{\pi D_{t,o}}, & \text{if } \theta = 0 \text{ or } 45^\circ \text{ (Square)} \\ 2\dfrac{\sqrt{3}\,P_t^2 - \dfrac{\pi}{2}D_{t,o}^2}{\pi D_{t,o}}, & \text{if } \theta = 60^\circ \text{ (Triangular)} \end{cases} \tag{17}$$

$$Re_s = \frac{\rho_s v_s D_{s,e}}{\mu_s} \tag{18}$$

The heat transfer coefficient for the shell side (h_s) is then computed from the Nusselt number in a similar way as Equation 14.

$$h_s = Nu_s \frac{k}{D_{s,e}} \tag{19}$$

Appendix B: Pressure Drop Modeling

For the tube side, the pressure drops are evaluated using the friction factor from the Gnielinski correlation [40]. Its expression is shown in Table A1. The pressure drop (ΔP_t) is then computed [43].

$$\Delta P_t = f_t \frac{L_t n_{t,pass} n_{ser} \rho_t v_t^2}{2 D_{t,i}} \tag{20}$$

For two-phase flows, the correlation from [44] is used. The pressure drop is computed as follows:

$$\Delta P_t = f L_t n_{t,pass} n_{ser} \left(\frac{\rho_{ex}^{-1} + \rho_{su}^{-1}}{D_{t,i}} + (\rho_{ex}^{-1} - \rho_{su}^{-1}) \right) G^2 \tag{21}$$

The two-phase friction factor f is computed using the two-phase number (K_f) and Re_l, the Reynolds number of the flow as if it was fully liquid (g is the gravitational constant):

$$f = 0.00506 Re_l^{-0.0951} K_f^{0.1554}, \quad K_f = \left| \frac{(x_{ex} - x_{su}) h_{vap}}{g L_t n_{t,pass} n_{ser}} \right| \tag{22}$$

For the shell side, the formulation from [5] is used with the formulation of the friction factor from [45].

$$f_s = 2 B_o Re^{-0.15} = 2 \times 0.72 \times Re^{-0.15} \tag{23}$$

$$\Delta P_s = n_{ser} f_s \frac{\rho_s v_s^2}{2} \frac{L_s}{B} \frac{D_{s,i}}{D_{s,e}} \tag{24}$$

Appendix C: Detailed Optimization Results

Tables A2 and A3 present the detailed optimization results for which:

- n_{disc} represents the number of heat exchanger discretization segments.
- t_t comp is set to `REF` when the tube thickness is calculated as $0.1 \times D_{t,o}$, and to `STD` when it is computed according to the standard described in Section 2.6.
- $n_{t,\text{pass}}$ choice is set to `=2` when maintaining the same value as in the reference cases, or to `OPT` when the optimizer selects the optimal value.

Table A2: Detailed optimization results compared with Case 1.

	Caputo	OPT1	OPT2	OPT3	OPT4	OPT5	OPT6	OPT7	OPT8
n_{disc}	1	1	1	1	1	30	30	30	30
t_t Comp.	REF	REF	REF	STD	STD	REF	REF	STD	STD
$n_{t,pass}$ choice	=2	=2	OPT	=2	OPT	=2	OPT	=2	OPT
$D_{s,i}$ [m]	0.83	0.89	0.64	0.79	0.64	0.94	0.94	0.94	0.94
L_t [m]	3.38	2.67	3.20	2.80	3.83	3.78	3.86	3.12	3.16
B [m]	0.5	0.89	0.64	0.56	0.64	0.76	0.77	0.63	0.63
$D_{t,o}$ [mm]	16	12.7	9.53	12.7	9.53	12.7	12.7	9.53	9.53
pitch ratio [-]	1.25	1.25	1.33	1.25	1.33	1.25	1.25	1.33	1.33
t_t [mm]	1.6	1.27	0.95	0.71	0.56	1.27	1.27	0.56	0.56
$D_{t,i}$ [mm]	12.8	10.2	7.62	11.3	8.41	10.2	10.2	8.41	8.41
n_t [-]	1567	2740	2182	2142	1892	3064	3064	4852	4852
n_{pass} [-]	2	2	1	2	1	2	2	2	2
BC [%]	25	28	30	30	38	35	40	39	38
θ [°]	60	60	60	60	0	60	60	60	60
A_{HX} [m^2]	262.8	292.1	208.6	239.5	217	462.7	471.8	453.7	458.8
α_t [W/m^{2}K]	3762	3638	4118	3739	3892	3390	3391	3157	3158
α_s [W/m^{2}K]	1740	1341	1731	1851	1528	1459	1444	1449	1440
$LMTD$ [K]	30.4	30.8	30.6	31.0	30.4	19.1	18.9	19.2	19.2
$\dot{Q}$ [kW]	4340	4363	4374	4343	4394	4341	4345	4340	4342
ΔP_t [Pa]	4298	3778	3443	3746	3317	4083	4156	3717	3755
ΔP_s [Pa]	13267	2449	6835	10684	5876	5230	5043	5070	4966
m_t [kg]	3009	2621	1404	1262	896	4151	4234	1873	1894
m_s [kg]	621	568	360	472	428	872	888	729	737
m_{ts} [kg]	116	150	61	105	69	177	177	191	191
m_B [kg]	36	16	14	22	18	34	32	37	37
m_{HX} [kg]	3782	3355	1839	1861	1411	5234	5331	2830	2859
$\frac{A_{HX}}{m_{HX}}$ [m^2/kg]	0.069	0.087	0.113	0.129	0.154	0.089	0.117	0.161	0.16
$\frac{A_{HX}}{V_{HX}}$ [m^2/m^3]	143.7	176.1	206.2	175.5	178.8	176.2	207.6	209.3	209.4

Table A3: Detailed optimization results compared with Case 2.

	Turgut	OPT1	OPT2	OPT3	OPT4	OPT5	OPT6	OPT7	OPT8
n_{disc}	1	1	1	1	1	30	30	30	30
t_t Comp.	REF	REF	REF	STD	STD	REF	REF	STD	STD
$n_{t,pass}$ choice	=2	=2	OPT	=2	OPT	=2	OPT	=2	OPT
$D_{s,i}$ [m]	0.17	0.25	0.25	0.25	0.25	0.25	0.25	0.25	0.25
L_t [m]	4.18	3.64	3.42	3.54	3.29	3.26	3.26	3.30	3.26
B [m]	0.38	0.36	0.35	0.34	0.33	0.33	0.33	0.33	0.33
$D_{t,o}$ [mm]	10	9.53	9.53	9.53	9.53	9.53	9.53	9.53	9.53
pitch ratio [-]	1.25	1.33	1.33	1.33	1.33	1.33	1.33	1.33	1.33
t_t [mm]	1	0.95	0.95	0.56	0.56	0.95	0.95	0.56	0.56
$D_{t,i}$ [mm]	8	7.62	7.62	8.41	8.41	7.62	7.62	8.41	8.41
n_t [-]	230	326	326	326	326	326	326	326	326
n_{pass} [-]	2	2	1	2	1	2	2	2	2
BC [%]	25	23	40	27	39	35	34	35	31
θ [°]	60	60	60	60	60	60	60	60	60
A_{HX} [m^2]	30.2	35.5	33.3	34.5	32.1	31.8	31.8	32.2	31.8
α_t [W/m^{2}K]	3743	3665	3643	4732	3376	3705	3882	3187	3178
α_s [W/m^{2}K]	4719	3064	3049	2948	3115	3148	3140	3118	3148
$LMTD$ [K]	10.9	9.9	10.2	9.8	10.3	10.4	10.2	10.2	10.4
$\dot{Q}$ [kW]	313	313	314	313	314	313	313	313	313
ΔP_t [Pa]	21755	11061	1231	12278	673	15795	15026	9456	9826
ΔP_s [Pa]	8235	3515	3911	3717	4202	4260	4277	4182	4258
m_t [kg]	213	239	224	143	132	214	214	133	131
m_s [kg]	55	81	76	78	73	72	72	73	73
m_{ts} [kg]	0.7	3	3	3	3	4	4	4	3
m_B [kg]	0.9	5	4	5	4	4	4	4	4
m_{HX} [kg]	270	328	307	229	212	294	294	214	211
$\frac{A_{HX}}{m_{HX}}$ [m^2/kg]	0.072	0.108	0.108	0.15	0.151	0.108	0.108	0.151	0.15
$\frac{A_{HX}}{V_{HX}}$ [m^2/m^3]	143.7	192.5	192.5	192.5	192.5	192.5	192.5	192.5	192.5

References

[1] S. Kakaç, H. Liu, A. Pramuanjaroenkij, Heat Exchangers - Selection, Rating and Thermal Design.

[2] A. H. Upadhyay, D. U. Vashisht, A. Dhall, P. Diwakar, J. Juneja, A REVIEW ON HEAT EXCHANGER DESIGN 3 (3).

[3] S. P. Boyd, L. Vandenberghe, Convex optimization, Cambridge University Press, Cambridge, UK ; New York, 2004.

[4] S. Katoch, S. S. Chauhan, V. Kumar, A review on genetic algorithm: past, present, and future, Multimedia Tools and Applications 80 (5) (2021) 8091–8126. doi:10.1007/s11042-020-10139-6.
URL http://link.springer.com/10.1007/s11042-020-10139-6

[5] A. C. Caputo, P. M. Pelagagge, P. Salini, Heat exchanger design based on economic optimisation, Applied Thermal Engineering 28 (10) (2008) 1151–1159. doi:10.1016/j.applthermaleng.2007.08.010.
URL https://linkinghub.elsevier.com/retrieve/pii/S1359431107002839

[6] A. L. Costa, E. M. Queiroz, Design optimization of shell-and-tube heat exchangers, Applied Thermal Engineering 28 (14-15) (2008) 1798–1805. doi:10.1016/j.applthermaleng.2007.11.009.
URL https://linkinghub.elsevier.com/retrieve/pii/S1359431107003936

[7] V. Patel, R. Rao, Design optimization of shell-and-tube heat exchanger using particle swarm optimization technique, Applied Thermal Engineering 30 (11-12) (2010) 1417–1425. doi:10.1016/j.applthermaleng.2010.03.001.
URL https://linkinghub.elsevier.com/retrieve/pii/S1359431110001080

[8] A. Ghanei, E. Assareh, M. Biglari, A. Ghanbarzadeh, A. R. Noghrehabadi, Thermal-economic multi-objective optimization of shell and tube heat exchanger using particle swarm optimization (PSO), Heat and Mass Transfer 50 (10) (2014) 1375–1384. doi:10.1007/s00231-014-1340-2.
URL http://link.springer.com/10.1007/s00231-014-1340-2

[9] O. E. Turgut, M. S. Turgut, M. T. Coban, Design and economic investigation of shell and tube heat exchangers using Improved Intelligent Tuned Harmony Search algorithm, Ain Shams Engineering Journal 5 (4) (2014) 1215–1231. doi:10.1016/j.asej.2014.05.007.
URL https://linkinghub.elsevier.com/retrieve/pii/S2090447914000756

[10] A. C. Caputo, P. M. Pelagagge, P. Salini, Heat exchanger optimized design compared with installed industrial solutions, Applied Thermal Engineering 87 (2015) 371–380. doi:10.1016/j.applthermaleng.2015.05.010.
URL https://linkinghub.elsevier.com/retrieve/pii/S1359431115004524

[11] J. Wen, H. Yang, G. Jian, X. Tong, K. Li, S. Wang, Energy and cost optimization of shell and tube heat exchanger with helical baffles using Kriging metamodel based on MOGA, International Journal of Heat and Mass Transfer 98 (2016) 29–39. doi:10.1016/j.ijheatmasstransfer.2016.02.084.
URL https://linkinghub.elsevier.com/retrieve/pii/S0017931015318238

[12] O. E. Turgut, Thermal and Economical Optimization of a Shell and Tube Evaporator Using Hybrid Backtracking Search—Sine–Cosine Algorithm, Arabian Journal for Science and Engineering 42 (5) (2017) 2105–2123. doi:10.1007/s13369-017-2458-6.
URL http://link.springer.com/10.1007/s13369-017-2458-6

[13] A. Hadidi, A. Nazari, Design and economic optimization of shell-and-tube heat exchangers using biogeography-based (BBO) algorithm, Applied Thermal Engineering 51 (1-2) (2013) 1263–1272. doi:10.1016/j.applthermaleng.2012.12.002.
URL https://linkinghub.elsevier.com/retrieve/pii/S1359431112008071

[14] M. Nadi, M. A. Ehyaei, A. Ahmadi, O. E. Turgut, MULTI-OBJECTIVE PARTICLE SWARM OPTIMIZATION OF THE K-TYPE SHELL AND TUBE HEAT EXCHANGER (CASE STUDY), Journal of Thermal Engineering 7 (3) (2021) 570–583. doi:10.18186/thermal.888261.
URL http://dergipark.org.tr/en/doi/10.18186/thermal.888261

[15] A. C. Caputo, A. Federici, P. M. Pelagagge, P. Salini, On the selection of design methodology for shell-and-tube heat exchangers optimization problems, Thermal Science and Engineering Progress 34 (2022) 101384. doi:10.1016/j.tsep.2022.101384.
URL https://linkinghub.elsevier.com/retrieve/pii/S2451904922001901

[16] Z. Xu, X. Ning, R. Li, X. Wan, C. Zhao, Configuration Optimization of a Shell-and-Tube Heat Exchanger with Segmental Baffles Based on Combination of NSGAII and MOPSO Embedded Grouping Cooperative Coevolution Strategy, Processes 11 (11) (2023) 3094. doi:10.3390/pr11113094.
URL https://www.mdpi.com/2227-9717/11/11/3094

[17] A. B. Krishna, K. Jin, P. S. Ayyaswamy, I. Catton, T. S. Fisher, Technoeconomic optimization of superalloy supercritical CO2 microtube shell-and-tube-heat exchangers, Applied Thermal Engineering 220 (2023) 119578. doi:10.1016/j.applthermaleng.2022.119578.
URL https://linkinghub.elsevier.com/retrieve/pii/S1359431122015083

[18] P. Prajapati, B. D. Raja, V. Patel, H. Jouhara, Energy-economic analysis and optimization of a shell and tube heat exchanger using a multi-objective heat transfer search algorithm, Thermal Science and Engineering Progress 56 (2024) 103021. doi:10.1016/j.tsep.2024.103021.
URL https://linkinghub.elsevier.com/retrieve/pii/S2451904924006395

[19] M. J. Bagajewicz, H. Hajabdollahi, A. Costa, Novel Global Optimization Approach for the Simultaneous Design of Heat Exchangers in Heat Exchanger Networks Constrained by Pressure Drop (2025). doi:10.2139/ssrn.5178889.
URL https://www.ssrn.com/abstract=5178889

[20] Z. J. Mosqueda-Huerta, O. D. Lara-Montaño, F. I. Gómez-Castro, M. Toledano-Ayala, Design and optimization of shell-and-tube heat exchangers through ANN and H-ANN models, Chemical Engineering Research and Design 220 (2025) 75–85.

doi:10.1016/j.cherd.2025.06.039.
URL https://linkinghub.elsevier.com/retrieve/pii/S0263876225003399
[21] G. F. Nellis, S. A. Klein, Heat transfer, 1st Edition, Cambridge University Press, Cambridge, 2012.
[22] M. Imran, R. Pili, M. Usman, F. Haglind, Dynamic modeling and control strategies of organic Rankine cycle systems: Methods and challenges, Applied Energy 276 (2020) 115537. doi:10.1016/j.apenergy.2020.115537.
URL https://linkinghub.elsevier.com/retrieve/pii/S0306261920310497
[23] S. Gürgen, Shell and tube heat exchanger optimization: A critical literature assessment and fairness-based comparative performance analysis of meta-heuristic algorithms, Case Studies in Thermal Engineering 72 (2025) 106405. doi:10.1016/j.csite.2025.106405.
URL https://linkinghub.elsevier.com/retrieve/pii/S2214157X25006653
[24] J. F. Schutte, J. A. Reinbolt, B. J. Fregly, R. T. Haftka, A. D. George, Parallel global optimization with the particle swarm algorithm, International Journal for Numerical Methods in Engineering 61 (13) (2004) 2296–2315. doi:10.1002/nme.1149.
URL https://onlinelibrary.wiley.com/doi/10.1002/nme.1149
[25] E. Neven, B. Chaudoir, V. Lemort, LABOTHAPPY: DEVELOPMENT OF AN OPEN-SOURCE PYTHON LIBRARY FOR THERMODYNAMIC SYSTEM MODELLING AND SIMULATION, in: Carnot Symposium 2024 Proceedings, Liège, 2024.
[26] B. B. Benuwa, B. Ghansah, D. K. Wornyo, S. A. Adabunu, A Comprehensive Review of Particle Swarm Optimization, International Journal of Engineering Research in Africa 23 (2016) 141–161. doi:10.4028/www.scientific.net/JERA.23.141.
URL https://www.scientific.net/JERA.23.141
[27] J. Primo, Shell and Tube Heat Exchangers Basic Calculations.
[28] J. E. Edwards, DESIGN AND RATING SHELL AND TUBE HEAT EXCHANGERS.
[29] R. C. Byrne, STANDARDS OF THE TUBULAR EXCHANGER MANUFACTURERS ASSOCIATION.
[30] J. E. Meyer, J. Frey, ASME Piping Code: B31.1, Power Pipingdoi:10.1115/1.861318_ch35.
URL https://asmedigitalcollection.asme.org/ebooks/book/238/chapter/14785272/ASME-Piping-Code-B31-1-Power-Piping
[31] ASME BPVC IV (2007), Boiler & Pressure Vessel Code, Rules for Construction of Heating Boilers, as required by the States of Alaska, Arizona, California, Illinois, Iowa, Kansas, Michigan, Missouri, Nebraska, New Hampshire, New Jersey, North Dakota, Ohio, Oregon, Utah, Wisconsin, et. alia. (2007).
URL chrome-extension://efaidnbmnnnibpcajpcglclefindmkaj/https://ia800805.us.archive.org/19/items/gov.law.asme.bpvc.iv.2007/asme.bpvc.iv.2007.pdf
[32] R. D. Beldar, S. Komble, Mechanical Design of Shell and Tube Type Heat Exchanger as per ASME Section VIII Div.1 and TEMA Codes for Two Tubes 8 (7).
[33] D. R. Moss, M. Basic, Pressure vessel design manual, 4th Edition, Elsevier/Butterworth-Heinemann, Amsterdam Boston, 2013.
[34] I. H. Bell, S. Quoilin, E. Georges, J. E. Braun, E. A. Groll, W. T. Horton, V. Lemort, A generalized moving-boundary algorithm to predict the heat transfer rate of counterflow heat exchangers for any phase configuration, Applied Thermal Engineering 79 (2015) 192–201. doi:10.1016/j.applthermaleng.2014.12.028.
URL https://linkinghub.elsevier.com/retrieve/pii/S1359431114011570
[35] I. H. Bell, J. Wronski, S. Quoilin, V. Lemort, Pure and Pseudo-pure Fluid Thermophysical Property Evaluation and the Open-Source Thermophysical Property Library CoolProp, Industrial & Engineering Chemistry Research 53 (6) (2014) 2498–2508. doi:10.1021/ie4033999.
URL https://pubs.acs.org/doi/10.1021/ie4033999
[36] CheGuide - LMTD Correction Factor Charts.
URL https://cheguide.com/lmtd_charts.html
[37] VDI e. V. (Ed.), VDI Heat Atlas, Springer Berlin Heidelberg, Berlin, Heidelberg, 2010.
URL https://link.springer.com/10.1007/978-3-540-77877-6
[38] X. Sui, W. Wang, C. Liu, P. Dong, Approximating printed circuit heat exchangers dynamics in a sCO2 RCBC as a low-order system via an optimal time constant, International Communications in Heat and Mass Transfer 157 (2024) 107771. doi:10.1016/j.icheatmasstransfer.2024.107771.
URL https://linkinghub.elsevier.com/retrieve/pii/S0735193324005335
[39] K. Bayramoğlu, I. Kaya, Y. Ust, Discrete thermal analysis of the E–type shell–and–tube heat exchanger, Scientific Reportsdoi:10.1038/s41598-026-35215-z.
URL https://www.nature.com/articles/s41598-026-35215-z
[40] S. M. Ammar, C. W. Park, Validation of the Gnielinski correlation for evaluation of heat transfer coefficient of enhanced tubes by non-linear regression model: An experimental study of absorption refrigeration system, International Communications in Heat and Mass Transfer 118 (2020) 104819. doi:10.1016/j.icheatmasstransfer.2020.104819.
URL https://linkinghub.elsevier.com/retrieve/pii/S073519332030347X
[41] F. P. Incropera, F. P. Incropera (Eds.), Fundamentals of heat and mass transfer, 6th Edition, John Wiley, Hoboken, NJ, 2007.
[42] H. Kücük, M. Ünverdi, M. Senan Yılmaz, Experimental investigation of shell side heat transfer and pressure drop in a mini-channel shell and tube heat exchanger, International Journal of Heat and Mass Transfer 143 (2019) 118493. doi:10.1016/j.ijheatmasstransfer.2019.118493.
URL https://linkinghub.elsevier.com/retrieve/pii/S0017931019321854
[43] D. Q. Kern, Process heat transfer, McGraw-Hill, New York, NY, 1950.
[44] J. Y. Choi, GENERALIZED PRESSURE DROP CORRELATION FOR EVAPORATION AND CONDENSATION IN

SMOOTH AND MICRO-FIN TUBES.
[45] M. S. Peters, K. D. Timmerhaus, R. E. West, R. E. West, Plant design and economics for chemical engineers, 5th Edition, McGraw-Hill chemical engineering series, McGraw-Hill, Boston, 2004.